GEORG-AUGUST-UNIVERSITÄT
GÖTTINGEN

II. Physikalisches Institut

Performance Study of DEPFET Pixel Detector Prototypes for Future Lepton Colliders Conducted at Beam Tests

von

Christian Geisler

To fully exploit the physics potential for future lepton colliders, a vertex reconstruction with unprecedented precision is needed. The depleted p-channel field-effect transistor (DEPFET) combines radiation detection and in-pixel amplification into a low noise particle detector. This thesis will present a detailed characterization of three different DEPFET pixel detector prototypes and their readout chain in a beam test environment. Eventually, the measured responses of the detector will be utilized to validate a DEPFET model used as a digitizer stage for Monte Carlo simulations.

Post address:
Friedrich-Hund-Platz 1
37077 Göttingen
Germany

Göttingen University
September 2010

GEORG-AUGUST-UNIVERSITÄT
GÖTTINGEN

II. Physikalisches Institut

Performance Study of DEPFET Pixel Detector Prototypes for Future Lepton Colliders Conducted at Beam Tests

von

Christian Geisler

Dieser Forschungsbericht wurde als Diplomarbeit von der Fakultät für Physik der Georg-August-Universität zu Göttingen angenommen.

Angenommen am:	22. September 2010
Referent:	Prof. Dr. Ariane Frey
Korreferent:	PD Dr. Jörn Grosse-Knetter

Und in der Mitte des Schrottplatzes, magische Träume erzeugend, lag das bebende, brummende Raumschiff. Rüttelnd und fauchend, die wieder angeschnallten Kinder wie Fliegen in einem Spinnennetz schaukelnd.

aus „Das Raumschiff"
von Ray Bradbury

Contents

Abstract and Outline

To fully exploit the physics potential for future lepton colliders, a vertex reconstruction with unprecedented precision is needed. The depleted p-channel field-effect transistor (DEPFET) combines radiation detection and in-pixel amplification into a low noise particle detector. A vertex detector based on the DEPFET technology meets the requirements of high pointing resolution and low material budget set by the linear collider ILC or the Belle II experiment at the B-factory SuperKEKB. This thesis will present a detailed characterization of three different DEPFET pixel detector prototypes and their readout chain in a beam test environment. Eventually, the measured responses of the detector will be utilized to validate a DEPFET model used as a digitizer stage for Monte Carlo simulations.

This thesis is organized as follows: Chapter 1 describes the context within which this study is conducted. It will shed light on the open questions that will be addressed with investigations at the latest generation of particle accelerators. Chapter 2 provides the mathematical description of the interaction of charged particles and matter, which is the basic process whereby signal is created in the studied detector. The scope of chapter 3 is the working principle of the DEPFET active pixel sensor, alongside a brief explanation of the underlying technology. Chapter 4 summarizes the experimental setup which allows studying the sensor prototypes as a part of a high-precision tracking telescope. In chapter 5 a detailed description of the data processing, with an emphasis on clustering and on position-finding algorithms, is given. Chapter 6 derives the physical properties of the devices under test from the preprocessed data. Furthermore, links between the measurements and the different design concepts of the prototypes are drawn. Finally, the acquired understanding of the sensor response is used in chapter 7 to validate a DEPFET model by comparing characteristic values of the experiment to the predictions of the model.

1 Context

Since the beginning of the 20th century exeriments have been performed to craft our understanding of the sub-atomic structure and interactions of the elementary particles. This chapter will briefly present the latest generation of particle colliders and the open questions that motivate the ongoing immense global effort in the field of particle physics.

1.1 Standard Model of Particle Physics

To our present understanding the basic constituents of matter are twelve spin 1/2 particles along with their antiparticles. These so-called fermions are further classified by their charge into leptons and quarks. The Standard Model incorporates three basic interactions of these particles. They are the strong, electromagnetic, and weak forces, all of which are mediated by spin 1 particles called gauge bosons. All fermions and gauge bosons have been observed in high energy experiments which accounts for the success of the Standard Model. Alone the process by which the particles acquire mass, the Higgs mechanism, which is boldly hypothesized has not been experimentally verified. With the latest generation of accelerators the exploration of the particle landscape at the Terascale (energies of teraelectron volts) will be possible. These experiments at the energy frontier will not only allow to test the Higgs hypothesis, but also adress a much broader set of open questions.

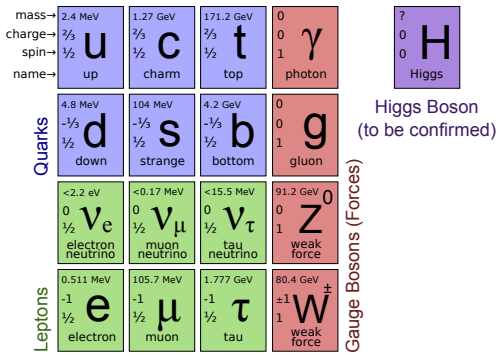

Figure 1.1: The particle content of the Standard Model of Particle Physics. The postulated Higgs boson is the only particle that has not yet been observed.

1.2 Large Hadron Collider

The Large Hadron Collider (LHC), with a budget of €7.5 billion, is one of the most expensive scientific instruments built by mankind.

The proton-proton collider is located at the European particle physics laboratory CERN in Geneva. The storage ring of the LHC has a circumference of 27 km and stores hadrons at a nominal center of mass energy of 14 TeV. The LHC houses the four experiments ATLAS, CMS, ALICE and LHCb, which will allow measurements on a wide variety of physics phenomena. The physics program includes precision measurements of the top quark and of the CP violation as well as searches for the Higgs boson and supersymmetry.

A clear disadvantage of hadron colliders is the uncertain initial state energy of the hard interaction, which limits the precision of measurements. In contrast, the precise knowledge of the initial state is the main advantage of lepton colliders.

1.3 International Linear Collider

The International Linear Collider (ILC) is a proposed project for a lepton accelerator that will collide electrons and positrons at energies of 500 GeV[1] (cf. figure 1.2). The clean initial state and benign environment will allow to extend and complement the physics program of the LHC.

The design of the International Large Detector (ILD) combines excellent calorimetry and tracking to obtain the best possible overall event reconstruction. This requires high spatial resolution for all detector sys-

[1]The design allows an upgrade to 1 TeV.

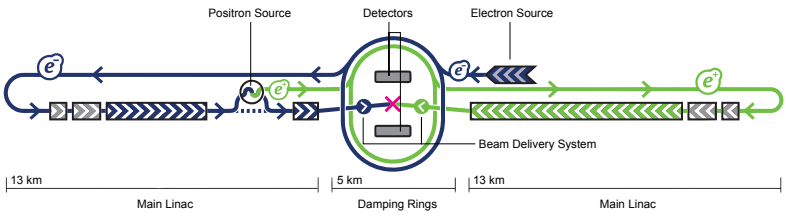

Figure 1.2: Schematic layout of the ILC complex for 500 GeV CM. Electrons and positrons will collide in the interaction region after acceleration by TESLA superconducting radio frequency units [B+07a].

tems. A highly granular calorimeter system is combined with a central tracker, which stresses redundancy and efficiency. In addition, excellent momentum resolution for charged particles and efficient reconstruction of secondary vertices are essential for an ILC detector [A+10b]. The latter aspect is strongly influenced by the properties of the innermost detector layer called the vertex detector (VTX).

The performance of the vertex reconstruction depends on the measurement accuracy of the shortest distance of a particle trajectory from the primary vertex. This impact parameter resolution depends on the VTX pointing resolution, lever arms, and mechanical stability, as well as on multiple scattering effects. The VTX is driven by these requirements and is optimized for excellent point resolution and minimum material thickness. Due to its intrinsic properties, which will be discussed in detail in chapter 3, the DEPFET concept has been proposed as one of the candidates for the underlying technologies of the VTX.

1.4 Belle II Experiment

The search for "new physics" is conducted by testing the Standard Model at extreme energies as done at the LHC or with high precision measurements at lower energies, which are possible at lepton colliders.

1.4.1 CP Violation

The violation of the invariance of the combination of charge conjugation and parity transformation (C,P) was first observed by Cronin and Fitch in the K_S,K_L system in 1964 [CCFT64] (Nobel prize 1980). The CP violation is equivalent to a difference in the decay pattern of particle and antiparticle, and is essential for the understanding of the surplus of matter over antimatter in the universe. In 1973 Kobayashi and Maskawa (Nobel prize 2008) proposed a theory describing the CP violation by a transformation of the three quark generations [KM73]. The elements of the transforming CKM-matrix are the couplings of down and up-type quarks. The unitarity constraints of the matrix can be displayed by six triangles, whose area is nonvanishing in the case of CP violation. Predictions from the Standard Model, which incorporates the KM-theory can be compared to measurements of these triangles to test the theory. The largest angles are found in the unitary triangles of the B-mesons (cf. figure 1.3), which are measured at asymmetric lepton colliders like the BaBar experiment

at the PEP-II collider at SLAC or the Belle experiment at KEK. These dedicated colliders are called *B-factories*.

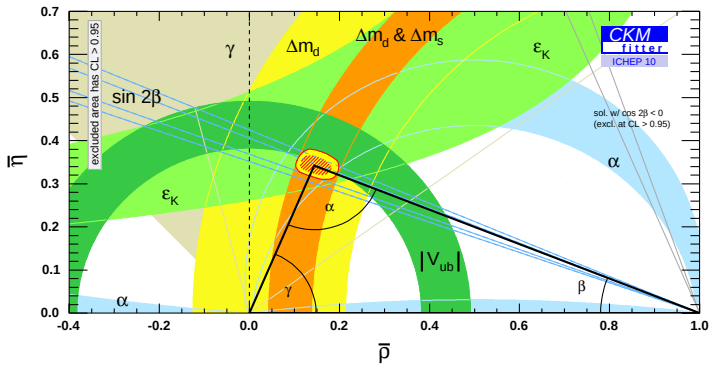

Figure 1.3: Confidence levels of the mixing angles of CKM-matrix for the global CKM fit. The shaded areas indicate the regions of $\leq 5\%$ CLs. The hatched area in the center of the combined fit result indicates the region where theoretical errors dominate [CHL$^+$05].

1.4.2 SuperKEKB and Belle II

SuperKEKB is the upgrade of the KEKB B-factory in Tsukuba, Japan. Like its predecessor, SuperKEKB is a ring-accelerator that will collide electrons at 8 GeV with positrons at 3.5 GeV in order to produce boosted Υ mesons that predominantly decay into B mesons. In the last decade, the experiment Belle at KEKB has proven the CP violation of the B mesons according to the CKM-theory. However, for a detailed test of the Standard Model the luminosity of the B-factory has to be increased to improve the precision of the measurements. SuperKEKB is designed to have a 40 times higher luminosity than KEKB and will lower the experimental uncertainties by almost one order of magnitude within the first six years of operation [Kie10].

To maintain the measuring precision in the harsh background environment caused by the increase in luminosity, the detector must also be upgraded. The installation of the Belle II detector will be finished in 2014 and will surpass the performance of its predecessor in several aspects including an improved vertex resolution, particle identification and energy resolution. The vertex reconstruction is mostly limited by multiple scattering from the detector, thus the minimal use of material and a short

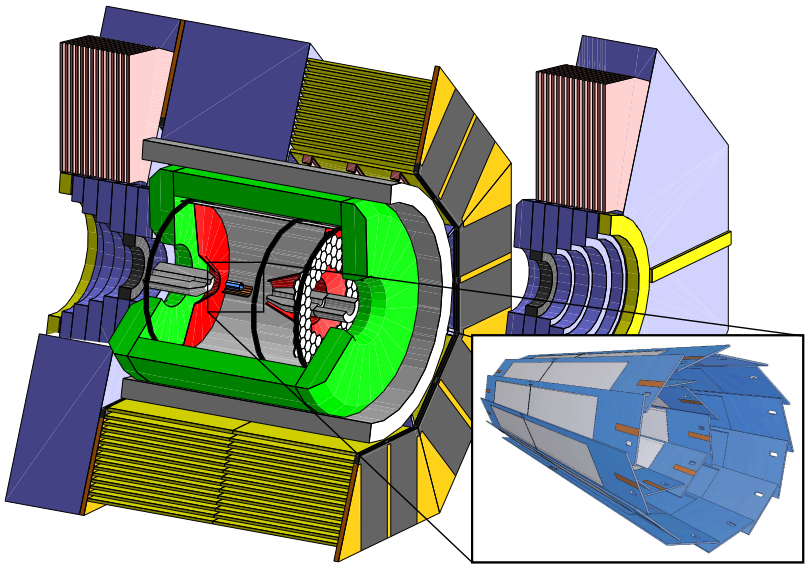

Figure 1.4: Design of the Belle II detector. The closeup shows the DEPFET pixel vertex detector. The other sub-detector components are (from inside out) the silicon strip sensors, central drift chamber, electromagnetic calorimeter and the K_L/μ detector [H$^+$04].

distance between interaction point and the first detector layer are both imperative. To suit these needs a pixel vertex detector (PXD) based on the DEPFET technology is currently under development by an international collaboration [DEP10]. The institutes forming the DEPFET collaboration are located in Germany[2], Spain[3], Poland[4] and the Czech Republic[5].

[2]Universities of Bonn, Gießen, Göttingen, Heidelberg and KIT Karlsruhe as well as the MPI München
[3]Universities of Barcelona, Ramon LLul, Santander and València and CNM Barcelona
[4]PAN Kraków
[5]Charles University Praha

2 Interaction of Charged Particles with Matter

Particles and radiation are detectable through their interaction with matter. This chapter will discuss the ionization and excitation of a material by an impinging charged particle, which is the dominant process whereby signal is created in a silicon sensor.

2.1 Stopping Power

The stopping power of a material is defined as the average energy loss per unit path length which charged particles suffer when traversing the material, as a result of Coulomb interactions with electrons and atomic nuclei. For particles heavier than electrons the predominant contribution to the total stopping power comes from inelastic collisions with electrons. The radiative stopping power, which is important for electrons, is negligibly small for protons or pions because it is inversely proportional to the square of the mass of the charged particle.

The dependence of the stopping power on the density of the medium ρ is largely removed by expressing the stopping power in units of $\mathrm{MeV}/(\mathrm{g}/\mathrm{cm}^2)$. The mass electronic stopping power is defined in terms of the inelastic scattering differential cross section $d\sigma_{in}(W,T)/dW$ for collisions with atomic electrons:

$$\frac{1}{\rho}S_{col}(T) = NZ\int_0^{W_m} W\frac{d\sigma_{in}}{dW}dW \tag{2.1}$$

where T is the initial kinetic energy and W the energy loss of the incident particle. The upper limit of the integration, W_m, is the largest possible energy loss in an elastic collision with an atomic electron. N is the number of atoms per gram of material, and Z is the number of electrons per atom.

2.1.1 Bethe Theory for Heavy Particles

Bethe [Bet30] used the relativistic Rutherford cross section and Born approximation to derive the differential scattering cross section of a heavy and fast particle. Various refinements to Bethe's theory have been developed [ICR93, ICR84, Ste82, Fan63, Jac98] and successfully tested experimentally [Ait69, All80, Bic88]. The so-called Bethe-Bloch equation, describing the specific average energy loss due to ionization, can be written in the form

$$(1/\rho)S_{col} = -(1/\rho)\left\langle dE/dx\right\rangle = \frac{4\pi r_e^2 mc^2}{\beta^2}\frac{1}{u}\frac{Z}{A}z^2 L(\beta), \tag{2.2}$$

where $r_e = e^2/mc^2$ is the classical electron radius, mc^2 is the electron rest energy, u is the atomic mass unit, $\beta = v/c$ is the particle velocity in units of the velocity of light, Z and A are the atomic number and relative atomic mass of the target atom, and z is the charge number of the projectile.

The quantity L is called the stopping number. The factors preceding the stopping number take into account the gross features of the energy-loss process, whereas L takes into account the fine details. $L(\beta)$ can be expressed as the sum of three terms:

$$L(\beta) = L_0(\beta) + zL_1(\beta) + z^2 L_2(\beta). \tag{2.3}$$

The first term is given by

$$L_0(\beta) = \frac{1}{2}\ln\left(\frac{2mc^2\beta^2 W_m}{1-\beta^2}\right) - \beta^2 - \ln I - \frac{C}{Z} - \frac{\delta}{2}, \tag{2.4}$$

where I is the mean excitation energy of the medium, C/Z is the shell correction, and $\delta/2$ the density effect correction. W_m is the maximum energy transfer possible in a single collision, given by

$$W_m = \frac{2mc^2\beta^2}{1-\beta^2} \times \left[1 + 2(m/M)(1-\beta^2)^{-1/2} + (m/M)^2\right]^{-1}, \tag{2.5}$$

where m/M is the ratio of the electron mass to the mass of the incident particle and mc^2 is the electron rest energy. In the case of relativistic pions the square brackets can be approximated to unity. Figure 2.1 shows the average energy loss in silicon due to ionization according to the Bethe theory for a charged pion. The mean mass stopping power for pions at 120 GeV used in the following detector characterization calculates to $2.55 MeV/(g/cm^2)$. Particles in the vicinity of the minimum ionization in the Bethe-Bloch approximation are called *minimum ionizing particles* (MIP).

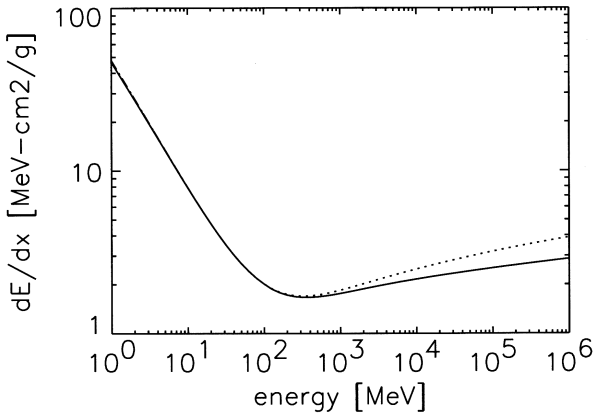

Figure 2.1: Specific average energy loss of charged pions in silicon as a function of the kinetic energy with (solid line) and without (dotted line) density and shell corrections [Lut99].

Mean Excitation Energy

The mean excitation energy is the main parameter of the stopping power formula and represents the logarithmic mean over the excitation energies E_n weighted according to the corresponding oscillator strengths f_n and is defined by [Fan63]

$$\ln I = \Sigma_n f_n \ln E_n. \tag{2.6}$$

The energy I therefore is independent of the properties of the projectile, and depends only on the properties of the material. In general ab initio calculations of I have only been done for atomic gases with low atomic numbers. In practice, I is extracted from experimental data. The most frequent method of obtaining the mean excitation values is by fitting the stopping power formula to measured stopping powers or ranges. The estimated value for silicon $I = 173eV$ used in this work is based on information from stopping-power measurements for protons, deuterons and alpha particles, as well as from oscillator strength distributions and dielectric-response functions given in ICRU report 37 [ICR84].

Density Effect

The density effect accounts for the polarization of the material through the passage of the charged particle. It is a relevant contribution to the stopping power only if the kinetic energy of the projectile is of the same order or larger than its rest energy. In this case the electric field flattens and

extends significantly, leading to an increased distant-collision contribution as $\ln(\beta\gamma)$ and a polarization of the media, limiting the field extension and effectively truncating this part of the logarithmic rise. In the case of highly relativistic particles ($\beta\gamma > 740$) an asymptotic function for $\delta(\beta)$ was given by Sternheimer [Ste82]:

$$\begin{aligned} \delta(\beta) &= \ln\gamma^2 - \ln(I/\hbar\omega_p)^2 - 1 \\ &= \ln\gamma^2 - 4.447 \end{aligned} \tag{2.7}$$

with the Lorentz factor $\gamma = (1-\beta^2)^{-1/2}$ and the plasma frequency of the medium ω_p. For ultra relativistic $120GeV$ pions the density effect term $\delta = 9.06$.

Low Energy Corrections

The second and third terms of equation 2.3 take deviations from the first-order Born approximation into account and are important only at low projectile velocities [ICR93]. The Barkas correction $zL_1(\beta)$ is proportional to an odd power of the projectile charge, and makes the energy loss of a negatively charged particle somewhat smaller than the energy loss of a positive particle with the same mass and velocity. The Bloch correction was derived without the first-order Born approximation and adds the term $z^2L_2(\beta)$ to the Bethe theory. Both low energy corrections will not be considered in this thesis.

Shell Corrections

The stopping power formula derived by Bethe is based on the assumption that the projectile velocities are large compared to the velocities of the bound atomic electrons in the target atom. As the velocity of the projectile decreases, the interactions of the particles with the innermost shells are reduced. This reduction effect is introduced by the shell correction term C/Z and can be determined with various methods ranging from calculations of hydrogen-like wave functions [Bic83] to the fitting of measured stopping powers to a stopping-power formula with a parametrized shell correction [AZ77].

2.2 Energy-loss Straggling

A particle penetrating matter looses energy in numerous Coulomb collisions with the target material electrons. The total energy loss Δ of the

particle is a stochastic quantity whose first moment, the average energy loss $\langle\Delta\rangle$, is given by the Bethe theory as the product of the stopping power and the path length s. In the following discussion, methods of determining the underlying probability function $F(\Delta)$ for different absorber thicknesses will be presented. $F(\Delta)$ is the *energy straggling function* which is often referred to as the *Landau distribution*.

2.2.1 Bohr Theory for Long Path Lengths

For relatively thick absorbers the particle undergoes a great number of collisions in which all classes, including the less frequent ones with large energy losses, are well represented. The straggling function is symmetric and can be described by a Gaussian distribution [Boh48, Fan63],

$$F(\Delta, s) = (\Omega(s)\sqrt{2\pi})^{-1} \exp\left[-(\Delta - <\Delta>)^2/(2\Omega(s)^2)\right] \tag{2.8}$$

with a variance $\Omega(s)^2$. The variance of any straggling function is given by

$$\Omega(s)^2 = s \int_0^{W_m} W^2 q(W) dW \tag{2.9}$$

where $q(W)dW$ is the probability, per unit path length, that an inelastic collision will occur with an energy loss between W and $W + dW$. The quantity $q(W)$ is called the collision spectrum and is proportional to the inelastic scattering cross section. With the use of the relativistic Rutherford cross section the collision spectrum becomes

$$\frac{q(W)}{\rho} = \frac{k}{W^2} \tag{2.10}$$

with

$$k = 2\pi r_e^2 mc^2 z^2 NZ/\beta^2. \tag{2.11}$$

The variance of the straggling function is then

$$\Omega^2 = ksW_m. \tag{2.12}$$

This approximation holds if Ω is much larger than the maximum energy loss in a single collision W_m and if $\langle\Delta\rangle$ is small compared to the initial particle energy.

2.2.2 Landau Theory for Moderately Short Path Lengths

The straggling theory developed by Landau [Lan44, Fan63] allowed the calculation of the total energy loss in detectors of moderate thickness. The change in the distribution of the total energy deposition $F(\Delta, s)$ as a result of passing through a thin layer δs is given by

$$\begin{aligned} F(\Delta, s+\delta s) - F(\Delta, s) = \; & - \; \delta s \int_0^\infty \frac{q(W)}{\rho} F(\Delta, s) dW \\ & + \; \delta s \int_0^\Delta F(\Delta - W, s) \frac{q(W)}{\rho} dW. \end{aligned} \tag{2.13}$$

The first term is the product of the probability for an energy loss Δ before entering δs with the mean number of collisions in the thin layer $\delta s \int_0^\infty q(W)/\rho dW$. It represents the probability of an energy reduction from Δ to $\Delta - \varepsilon$ in the thin layer. The second term is the probability that the energy loss at s is $\Delta - W$ and a collision with energy reduction W occurred within δs. This equation may be put in the form of a transport equation

$$\frac{\partial F}{\partial s}(\Delta, s) = \int_0^\infty \frac{q(W)}{\rho} [F(\Delta - W, s) - F(\Delta, s)] dW, \tag{2.14}$$

which has been solved by Landau with the Laplace transform method. An approximation of the Landau distribution, with the use of the Rutherford cross section, is given by [Gru93]

$$F_L(\lambda) = \frac{1}{\sqrt{2\pi}} \exp\left[-\frac{1}{2} (\lambda + \exp(-\lambda)) \right], \tag{2.15}$$

with

$$\lambda = \frac{\Delta - \Delta_{mpv}}{\xi} \tag{2.16}$$

being the deviation from the most probable energy loss Δ_{mpv}. This approximation holds for thin absorbers, i.e. primarily gases, for which the Landau parameter ξ is given by

$$\xi = 2\pi N_A r_e^2 m_e c^2 z^2 \frac{Z}{A} \cdot \frac{1}{\beta^2} \rho s. \tag{2.17}$$

The Landau theory is applicable for intermediate path lengths where the typical energy deposit ξ is much greater than the mean excitation energy I and much smaller than the maximum energy loss W_m.

Hancock [HJM+83] extended the Landau theory by convoluting $F_L(\lambda)$ with a Gaussian distribution representing the resonance collisions which were disregarded with the use of the Rutherford cross section. With this modification the accuracy of the straggling function improved, particularly for short path lengths. In practice the Landau parameter ξ, the most probable energy loss Δ_{mpv} and the width of the Gaussian are adjusted until a good fit is obtained.

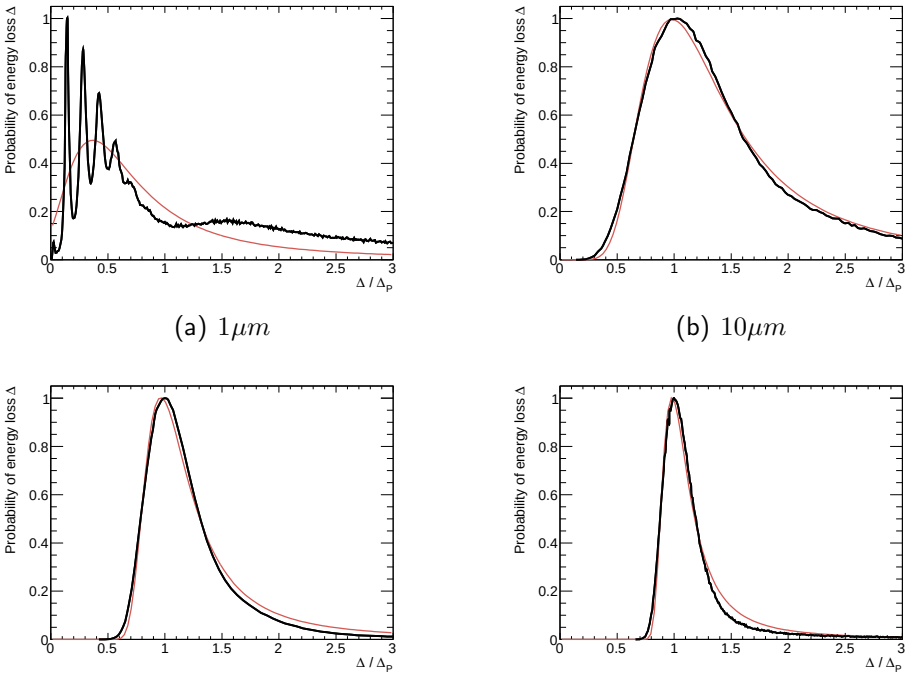

(a) $1\mu m$ (b) $10\mu m$

(c) $75\mu m$ (d) $450\mu m$

Figure 2.2: Straggling functions for various silicon detector thicknesses as obtained with a Monte Carlo simulation [Bic88] of particle passages with $\beta\gamma = 1000$ (black). For comparison a Landau distribution with the fitted Landau parameter ξ is shown (red). The separate peaks in the $1\mu m$ thick sensor, corresponding to plasmon excitations, are already merged by a thickness of $10\mu m$.

2.2.3 Calculations by Bichsel for Short Path Lengths

For the calculation of the energy-loss distribution in a plural scattering regime, involving fewer than about 100 collisions, an accurate description of the collision spectrum for low as well as for large losses must be used.

In the calculation of Bichsel [Bic88] the collision cross section consists of three contributions: (1) the longitudinal low-K excitation $\sigma_l(W)$, due to the unretarded static Coulomb interaction, (2) the transversal excitation $\sigma_t(W)$, due to the emission and reabsorption of virtual photons and (3) the contribution from large momentum transfers $\sigma_u(W)$. These collision spectra must be convoluted with a suitable numerical method.

The straightforward approach of calculating straggling functions is the Monte Carlo (MC) calculation. Here the passage of a particle through the material is simulated. Two random numbers from a uniform distribution, $\xi \in [0, 1)$ and $\zeta \in 1, 2, ..., 10000$, define the properties of the subsequent collisions. Those are (1) the distance traveled until the next collision occurs given as $-ln(\xi)/M_0$ with the number of collisions per unit path length $M_0 = 3.84312\mu m^{-1}$ at $\beta\gamma = 1000$ and (2) the momentum transferred to the struck electron given by the inverted collision spectrum $W(\zeta)$ for $\beta\gamma = 1000$ shown in figure 6.4 [1]. The individual energy losses are summed up to the total energy loss Δ. After many cycles of repetition the straggling function $F(\Delta, s)$ can be obtained.

Figure 2.2 displays straggling functions obtained with this model for different sensor thicknesses. The ξ of the landau distribution according to equation 2.15 has been fitted to the MC simulation and describes the energy straggling fairly well.

2.3 Energetic Knock-On Electrons

If the energy transport W of the projectile to an atomic electron largely exceeds the ionization energy I of the material, the hit electron will fork out and deposit energy away from the primary track. The number of these δ-rays of energy W_r or greater produced per cm of track can be approximated within a 10% error with the use of the Rutherford cross section by [Bic06]

$$\sigma_\delta(W_r) \approx 153 \frac{\rho Z}{\beta^2 A} \frac{1}{W_r}. \tag{2.18}$$

In the case of silicon the probability of producing a δ-ray with $W > 20keV$ $(100keV, 200keV)$ during the passage of the particle through a $450\mu m$ thick sensor is calculated to $40\%(8\%, 4\%)$.

[1] Since the high energy transfers are most important for the shape of the high signal tail of $F(\Delta)$ the corresponding region of the inverted collision spectrum is sampled with higher accuracy. If $\zeta > 9990$, a third random number ζ' determines the exact value of the high energy transfer (cf. dashed line in figure 6.4.).

T(keV)	R(Si)	T(keV)	R(Si)	T(keV)	R(Si)	T(keV)	R(Si)
0.1	0.004	2	0.10	20	3.0	200	160
0.2	0.008	4	0.24	40	10	400	450
0.4	0.015	7	0.55	70	27	700	960
0.7	0.030	10	0.96	100	50	1000	1520
1	0.04						

Table 2.1: Practical ranges R in μm of electrons with kinetic energy T in silicon. For $E > 50keV$ ranges were calculated with the algorithm given in Ref. [Kob68]. Between 10 and $50keV$, calculated ranges [Kob68] were reduced smoothly to the experimental value at $10keV$. The uncertainty in R is about 20%. Taken from [Bic06].

The determination of the range of the low energy electron is a difficult task due to the lack of accurate shell corrections, which are required if the velocity of the incident electron is in the same order of magnitude as the atomic electrons. For the estimation of the practical range of a low energy electron in a material the reduction by large angle scattering along the path has to be considered. Table 2.1 from [Bic06] collects practical ranges R of low momentum electrons in silicon. With the use of the tabulated values of R the probability for a δ-ray to carry signal charge further than $3\mu m(50\mu m, 160\mu m)$ can be estimated to $40\%(8\%, 4\%)$.

The angular distribution of a knock-on electron with kinetic energy W_e and corresponding momentum p_e is given by [A$^+$08]

$$\cos(\theta) = \frac{p_{max}}{p_e}\frac{W_e}{W_m}, \tag{2.19}$$

with p_{max} being the momentum of an electron with the maximum energy transfer possible in a collision W_m.

2.4 Multiple Scattering

Each collision of a particle traversing a material leads to a deflection of the primary track. The predominant contribution to this small angle scattering stems from the Coulomb interaction with the nuclei. The RMS of the projected angular distribution can be described using the Molière theory by

$$\Theta_{RMS}^{proj} = \frac{13.6MeV}{\beta cp} z\sqrt{\frac{x}{X_0}} \times [1 + 0.038\ln(x/X_0)], \tag{2.20}$$

with the thickness of the material in units of the radiation length x/X_0. For small scattering angles (central 98%), the distribution follows a Gaussian. For large angles scatting behaves like Rutherford scattering, with larger tails than expected for a Gaussian distribution [A+08].

The expected opening angle of a parallel 120 GeV pion beam traversing $450\mu m$ of silicon ($X_0 = 9.36cm$) is calculated to $6.26\mu rad$. The smearing in the spatial position is estimated to $1.7\mu m$ after the passage through the beam test setup described in section 4.2.

2.5 Ionization Yield

Ionization chambers and semiconductor counters respond to the passage of a charged particle with a signal proportional to the number of electron-hole pairs created in their sensitive volume. The number of separated charge pairs J is connected to the deposited energy Δ by the proportionality factor W [Fan63]

$$J = \Delta/W \tag{2.21}$$

The average energy needed for the formation of a electron-hole pair in silicon is $3.6eV$, more than three times larger than the band gap of $1.12eV$. The residue energy is dissipated as phonons and kinetic energy insufficient to produce ionization.

The low W values for solid state ionization chambers ($\mathcal{O}(1eV)$), which is a factor 10 smaller than the W value for gases ($\mathcal{O}(10eV)$), can be explained qualitatively by the broadening of the discrete energy levels into the valence and conduction band when distant atoms in a gas aggregate into the densely packed and correlated solid state.

A range of physical effects influence the W value. In the MeV range a dependency on the particle species, on the temperature of the material, and on the energy of the projectile, leading to a change in W in the percent level, have been observed. W further depends on the concentration of crystal defects. The W value of $3.6eV$ for silicon has been obtained from $8.78MeV$ alpha particles at $300K$ [ICR79].

3 Working Principle of the DEPFET Active Pixel Device

The depleted p-channel field-effect transistor (DEPFET) pixel detector is a silicon sensor able to register ionization created in the material by an impinging particle. The concept was proposed by Kemmer and Lutz in 1986 [KL87] and was experimentally verified in 1990 [KL$^+$90]. This chapter will summarize the basic properties of silicon and discuss the design and operation principle of the DEPFET sensor in greater detail.

3.1 Physics and Properties of Semiconductors

A semiconductor is a solid state crystal characterized by a small range of forbidden energy states adjacent to the energy states occupied by the valence electrons. This so-called band gap separates the valence band from the conduction band. For the semiconductor silicon the width of the band gap is $1.14eV$, for the isolator silicon oxide the gap of $9eV$ is much wider. According to the Fermi-Dirac theory the probability that an electron is in an energy state higher than the ground state is zero at $0K$, and increases with temperature. When the energy levels are occupied to 50%, this is referred to as the Fermi level E_f and characterizes the sudden drop in the occupation density. For pure (intrinsic) silicon E_f is approximately mid-band gap. At room temperature the thermal excitation is small compared to the band gap of silicon ($\approx 0.026eV$) and is the cause of the low conductivity.

3.1.1 Doped Semiconductors

In a doped (extrinsic) semiconductor tiny fractions (1 in 10^{11}) of the semiconductor atoms are replaced by atoms that have a different number of valence atoms. The dopant is bound covalently to the crystal lattice which presents a tetravalent bond leaving an excess electron in the case of a pentavalent dopant and a vacancy (hole) in the case of a trivalent dopant. The

former is an donor forming n-type material, and the latter is an acceptor leading to a p-type semiconductor. Donor doping raises E_f close to the conduction band and acceptor doping lowers E_f close to the valence band. Doping and the consequential shift of E_f results in a high concentration of free electrons or holes.

3.1.2 pn-Junction

Conducting materials in contact with one another must establish the same Fermi level E_f. Contact of n-type and p-type silicon leads to a diffusion current of electrons from the donors to the acceptors and of holes vice versa. In thermal equilibrium this current is compensated by a drift current caused by the electric field of the immobile dopant ions. The strength of the opposing field can be characterized by the so-called bias voltage. The region sweeped free of charge carriers is called the depletion zone.

An external voltage applied in the same direction as the bias voltage further removes free space charges and extends the depletion zone. An electron hole pair created by an impinging particle in the depleted silicon will be influenced by the electric field, gets separated, and each constituent will be drifted towards their potential minimum accordingly. The charge can be collected on segmented electrodes on the top and the back of the diode and allows the detection of the passage. The shape of the signal induced by the separated charges can be calculated with the Ramo theorem. A pn-junction operated in this reverse bias is therefore the fundamental building block of a silicon detector.

3.2 Depleted Field-Effect Transistor

The depleted p-channel field-effect transistor (DEPFET) represents the combination of a particle detector and an amplification structure.

3.2.1 Metal Oxide Semiconductor Field-Effect Transistor

The p-channel metal oxide semiconductor field-effect transistor structure (cf. figure 3.1 (b)) consists of three terminals on an n-type substrate, i.e. the source, gate, and drain. The source and drain regions are p^+-doped and the gate is insulated from the substrate by a thin oxide layer. The oxide prevents the flow of current from the gate and allows the build-up

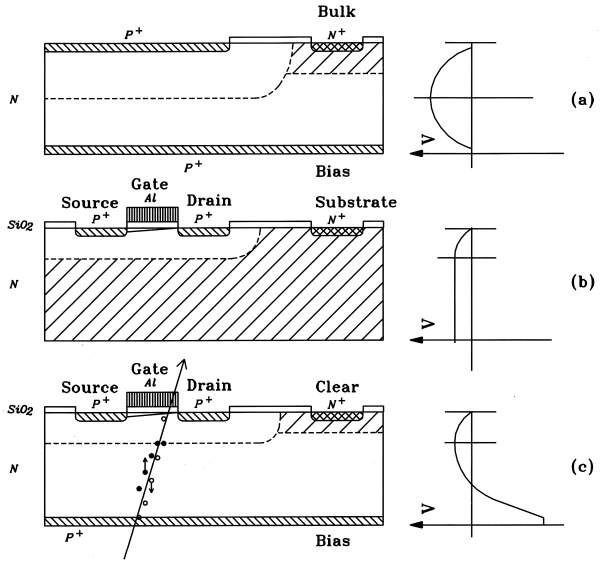

Figure 3.1: Concept of DEPFET detector-amplification structure (c) based on a sideward-depleted silicon bulk (a) with an embedded planar field effect transistor (b). The potential shape (right) assumes ground potential on the p^+ contacts on top and bottom surfaces and negative voltage on the n^+ bulk contact [Lut99].

of a negative electric field, which pushes the free electrons of the n-silicon beneath the gate contact into the bulk.

At positive or zero gate voltage (w.r.t. bulk) source and drain are insulated from each other. By applying a sufficient negative gate voltage, an inversion layer will form below the gate and establish a conductive connection between the source and drain regions. The conductivity of this channel can be controlled by the gate voltage. The MOSFET therefore is classified as a voltage-controlled transistor.

3.2.2 Sideward Depletion

The concept of sideward depletion was proposed by Gatti and Rehak [G+84] and is shown in figure 3.1 (a). By placing two p^+ electrodes on front and back and an n^+ contact on the offside of an n-conducting wafer, the bulk can be depleted sideways, which allows the reduction of the depletion voltage by a factor of four. By applying a negative (w.r.t. bulk) voltage to both p^+ contacts, the majority carriers are pushed to the n^+ bulk anode resulting in the growth of the depletion zone from both sides of the wafer. Accordingly, a potential minimum for majority carriers

(electrons in n-type silicon), attractive for the electrons, is formed within the silicon whose depth can be controlled by the ratio of the p^+ contact potentials.

3.2.3 Depleted p-Channel MOS Field-Effect Transistor

The combination of the MOSFET with the technique of sideward depletion allows the formation of a electrophile potential valley beneath the (external) gate of a MOSFET structure serving as a second (internal) gate. With an additional deep n-implantation the internal gate is laterally structured and shifted further into the proximity ($\approx 1\mu m$) of the conducting channel. The basic schematic of the resulting p-channel DEPFET device is shown in figure 3.1 (c).

Applying a negative voltage to the external gate results in the formation of the inversion layer and a conducting connection between source and gate. A charge pair created by an impinging particle in the depleted silicon bulk will be separated by the external electric field. While the hole will flow to the backside electrode, the electron will be collected in the internal gate, thereby modulating the transistor current by inducing mirror charges in the inversion layer. The strength of the current modulation is a measure of the electrons collected in the potential pocket which is proportional to the electron hole pairs created and proportional to the energy deposited by the particle in the sensor. The effect of a signal charge on the transistor current is characterized through the gain of the internal gate

$$g_q = \frac{\partial I_D}{\partial Q_{sig}} \tag{3.1}$$

which strongly depends on the length of the internal gate, its proximity to the channel, and on the capacitance of the oxide. DEPFET sensors with g_q values up to $688 pA/e^-$ have been produced and are examined in this work.

Signal electrons are captured in the internal gate and need to be removed to prevent the potential minimum, and thus the amplification stage, from saturating. This is accomplished by pulsing an n^+ doped clear electrode to a large positive voltage lowering the potential barrier between the internal gate and the clear contact (punch through) and thus allowing the flow of electrons towards the clear contact.

To avoid the loss of charge into the clear region during charge collection the clear electrode is shielded by a deep p-well implantation which rises the potential barrier between internal gate and clear region. This barrier

hinders the clearing and led to the introduction of a clear gate structure for the operation of the prototype sensors. The height of the potential barrier can be controlled by the clear gate voltage. The clear gate voltage is tuned to achieve a complete clearing of the internal gate while preventing the loss of signal charge into the clear region. All devices analyzed in this study, with the exception of one DUT (cf. section 4.4.2), are operated at a static clear voltage. This clear mode is referred to as the *common clear gate* configuration. A detailed description is given in [Rum09].

3.2.4 DEPFET Properties

When compared to the standard detector combination of a pn-diode and an external amplifier, several properties of the DEPFET device stand out. The most important feature for low noise applications (e.g. X-ray spectroscopy) is the intrinsic amplification of the detector, which reduces the noise by a factor of two in comparison to a two-stage combination. Parasitic capacities from the connection of detector and amplifier can be eliminated and reduction of the gate capacitance to very small values will increase amplification and further reduce serial noise. The noise contribution of a DEPFET structure to the signal peak of the K_α line from an ^{55}Fe source has been measured to $4.8e^-$ [K$^+$05]. In particle physics applications the excellent signal-to-noise performance allows the thinning of the sensor and the use of the DEPFET device as a highly permeable vertex detector. Thinning of the sensor to $75\mu m$ using deep anisotropic etching has been successfully demonstrated [A$^+$04] and will be used for the construction of the Belle II pixel vertex detector (PXD). The gated readout reduces the power consumption and therefore the need for cooling structures, which further qualifies the detector for low material budget applications. The drawback of the row-wise operation is the, for a collider experiment, relatively slow readout speed. The PXD of Belle II has a frame size of $\approx 8 \cdot 10^6$ pixel read out within $20\mu s$ and an estimated total power consumption of $360W$ [A$^+$10a].

3.3 Rolling Shutter Readout

The 16k DEPFET pixels of the sensor studied in this work are arranged in a rectangular matrix with 128 rows and 128 columns. The readout is performed in the so-called rolling shutter mode, which accesses the sensor row by row with the parallel readout of the pixel signals. The schematic

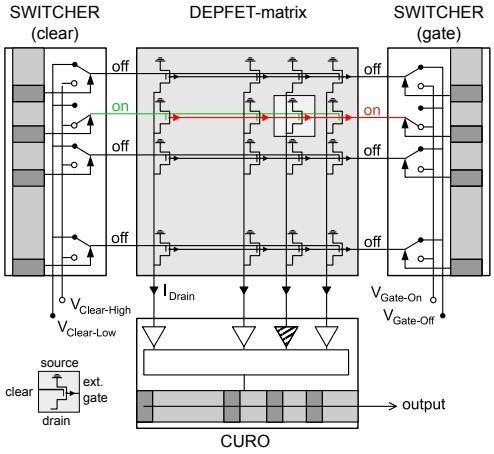

Figure 3.2: Principle of operation of a DEPFET pixel matrix [K+05]. The gates and clear contacts are multiplexed row-wise and steered by the SWITCHER ASIC, the drains are multiplexed in columns and connected to the CURO readout chip.

setup is shown in figure 3.2. Two application-specific integrated circuits (ASIC) are placed on the left and right side of the DEPFET sensor. The SWITCHER chip on one side has 128 output channels, each connected to the gates of one row. The 128 channels of the SWITCHER on the other side are connected to the row-wise clear contacts. The SWITCHER chips are designed to provide a fast ($\approx$ 10ns into 50pF) voltage pulse of up to 20V to the gate and clear lines. The current readout chip CURO is placed beneath the matrix and contains 128 input channels each connected to a column of multiplexed drains. The CURO ASIC is based on a current mode signal processing scheme. It buffers two currents, subtracts them, and pipes the result into two external transimpedance amplifiers (TIA).

Two loops have been used for reading out the pixel matrix, one for idle-clearing and one for the actual readout. They will be referred to as the clear cycle and the readout cycle. During the clear cycle the clear SWITCHER pulls the clear of one row after the other to a positive potential thereby clearing the internal gate from signal or leakage charges. After the clearing of row 128 the loop recommences at row 1. An external trigger can interrupt this otherwise infinite loop after each cleared row and start the rolling shutter readout cycle. The first row read after the arrival of a trigger signal will be called the *start-gate*. The double sampling readout loop steps through the 128 rows of the matrix, performing the following procedure:

1. The gate steering SWITCHER pulls the gate line and allows the pixel in the row to be read out. The drain currents I_D are stored in the current cells of the CURO.

2. The pixels in the row are cleared with a voltage pulse from the second SWITCHER to the clear contact.

3. After the clear, the drain current (post-clear) is subtracted from the buffered current (pre-clear) in the memory cells on the CURO. The Read-Clear-Read sequence of the row is completed if the differential signals have been processed by the CURO chip and the loop counter is incremented.

The pixel-wise currents are shifted out of the CURO, converted to a voltage signal, and digitized by an 14 bit analog to digital converter (ADC). The 64 currents form the drain channels of the left and right part of the matrix are converted to voltages and digitized by separate TIA and DAC. After all 128 rows have been read, the clear cycle begins again. The digital pixel values, run and event number, and the start gate row are saved in a run file. Figure 3.3 shows the schematics of the S3b readout board developed at the University of Bonn [Fur10]. The board is holding the sensor, ASIC and TIA in the top module and the downstream signal processing structures in the lower part.

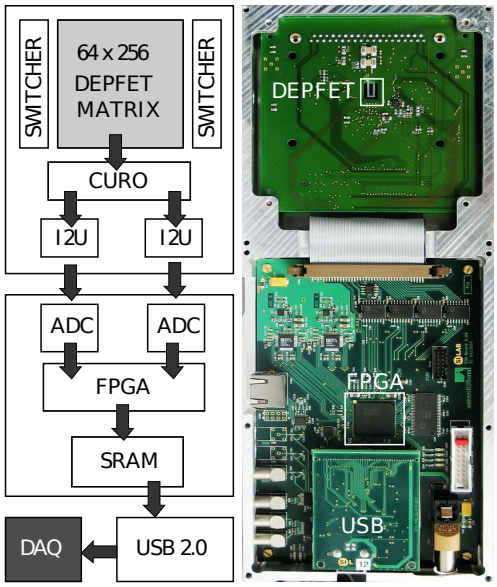

Figure 3.3: Block Diagram and photo of the readout board [Fur10]. The top part including the pixel matrix, ASIC, and TIA is called the hybrid. The lower part including the ADC, FPGA and USB controller is the DAQ board.

4 Beam Test Setup

The performance of three DEPFET prototypes developed for the ILC has been studied in a high energy pion beam. For the estimation of characteristics like the spatial resolution or the charge collection efficiency of a sensor prototype, the so-called device under test (DUT), a tracking telescope able to predict the position of a particles passage through the DUT has been employed. In this chapter, the experimental setup of the utilized beam telescope, the data acquisition, and the design properties of the DEPFET prototypes are presented.

4.1 Beam Properties

The testing of the DEPFET prototypes at the CERN super proton synchrotron (SPS) beam line H6 has been performed mainly in a beam of charged pions at 120GeV. Every 16.8 seconds protons are extracted from the ring accelerator. This so-called spill is collided with a wolfram target. The shower of secondary particles, mostly pions, is focused and channeled to the beam test area. The length of a spill is 4.8 seconds and the particle rate is $\approx$ 1kHz. The beam optics and mechanical alignment have been tuned to operate at the maximal readout rate of the sensors of $\approx$ 100Hz at an average occupancy of one to two hits per frame on the DUT.

Under the assumption of a Gaussian profile, the width of the beam and the RMS of the angular distribution have been measured to 3.6mm and 3mrad (cf. figure 5.16). The energy resolution of the pion beam is $\approx 1\%$.

4.2 Beam Telescope

The telescope used in the beam test of summer 2009 is shown in figure 4.1. It consisted of five DEPFET sensors, two up-stream and three down-stream of the DUT. The telescope as well as the DUT readout were triggered in the case of a coincidence of two scintillator signals from the front and the back of the telescope by the trigger logic unit (TLU).

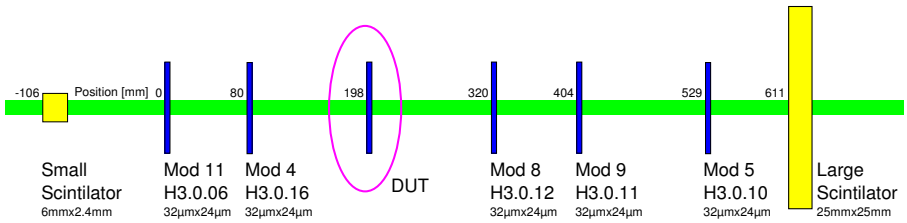

Figure 4.1: Schematic of beam test setup with six DEPFET sensors at CERN SPS during the summer 2009.

Each DEPFET sensor was attached to an separate x-y motor stage and could be aligned individually with the beam and with the other modules with a precision in the order of $1\mu m$. These motor tables together with the scintillators were mounted on a dedicated and robust aluminum table.

The telescope modules contain DEPFET chips studied in previous beam tests [K$^+$09], and their properties are well known. The $450\mu m$ thick silicon devices of the PXD5 production charge are structured in 64×256 pixel with a size of $32 \times 24\mu m^2$ resulting in a total size of $2.048 \times 6.144\text{mm}^2$. The sensors are designed in a double-pixel structure allowing the parallel readout of two rows and thus matching the 128×128 logic operation scheme explained in section 3.3. Neglecting misalignment and multiple scattering and taking the spatial resolution of the telescope sensors from [K$^+$09] as $\Delta x_{mod} = 2 \pm 0.5\mu m$ and $\Delta y_{mod} = 1.5 \pm 0.3\mu m$ the error on the predicted position in the DUT layer Δx_{tel} and Δy_{tel} is estimated to

$$\Delta x_{tel} = \Delta x_{mod} \frac{1}{\sqrt{5}} = 0.89 \pm 0.22\mu m \tag{4.1}$$

$$\Delta y_{tel} = \Delta y_{mod} \frac{1}{\sqrt{5}} = 0.67 \pm 0.13\mu m. \tag{4.2}$$

4.3 DAQ Prototype System

The digital data from the six readout boards is send to the event builder, which assembles a complete event from the six modules. This event is distributed by the event server to consumers like the *online-monitor* or the *file-writer* [Fur10].

4.3.1 Raw Data Format

The beam test data is saved in a binary format which is organized event by event.

- The first event in a run file is the *Begin of Run Event* (BORE) containing a description of the setup of the telescope and the DUT.
- There are two types of *Info Events* that contain either a unique run number or information from the TLU like the coincidence rate or the time stamp.
- A *Data Event* contains the six module headers storing information about the module, such as type, number, and trigger, and the six frames containing the pixel values from telescope and DUT.
- The end of run event (EORE) indicates the end of a run.

The 14 bit ADC values of the pixels are stored in a 2 byte word. The output of CURO after the readout of a pixel with a cleared internal gate is called the pedestal. To capture fluctuations in positive and negative direction the ADC is tuned so that the pedestal is sampled to $\approx$ 8000 ADC counts.

4.4 Devices Under Test

Three prototypes were studied during beam test session of 2009. All three modules were originally designed for the ILC and thus have relatively small pixel pitches. The devices differ in pixel pitch, internal gain, and the clear method. These differences manifest in signal-to-noise ratios and pointing resolution shown in table 4.1 and are discussed in greater detail in chapter 6. Like the telescope modules the prototypes pixel are arranged in 128 rows of 64 double pixels resulting in a physical size of 64×256 pixel. The arrangement of the double pixel allows the readout of two rows and the sampling of 128 pixel within one clock matching the operation scheme described in section 3.3. The metallization and implantation layers of the double-pixels are shown in figure 4.2. None of the DUT are thinned and have a thickness of $450 \mu m$.

DUT	S/N	g_q [nA/e$^-$]	dir.	P [μm]	Δd [μm]
STD	128.4 ± 2.8	379 ± 15	x	24	1.19 ± 0.16
			y	24	1.39 ± 0.06
C3G	148.4 ± 5.2	516 ± 21	x	32	1.55 ± 0.13
			y	24	1.51 ± 0.06
HiG	213.3 ± 7.7	688 ± 27	x	20	1.03 ± 0.19
			y	20	1.34 ± 0.07

Table 4.1: Signal-to-noise ratio S/N, in-pixel gain g_q, pixel pitch P and spatial resolution Δd of the DUT of 2009.

4.4.1 Standard Module

The standard module with the internal marking H3.0.04 is similar to the telescope modules but has a smaller pixel pitch of $24\mu m \times 24\mu m$ resulting in a reduced active area of $1.536 \times 6.144\text{mm}^2$. In this work, this DUT will be given the label "STD" since its performance has already been studied in the beam test session of 2008.

4.4.2 Capacitive Coupled Clear Gate Module

As stated in section 3.2.3 the standard operation mode includes a clear gate which is operated at a static potential. The DUT module with the marking H3.0.01 has a changed clear structure allowing the operation of the matrix with a clear gate voltage that is coupled capacitive to the clear contact. A positive voltage pulse on the clear contact will thus also cause a positive potential on the clear gate. This lowers the potential barrier between internal gate and clear region and facilitates the sweeping of the internal gate. The matrix with an active area of $2.048 \times 6.144\text{mm}^2$ and pixel dimensions of $32 \times 24\mu m^2$ will be labeled "C3G".

4.4.3 High Gain Module

The DUT module with the internal marking H3.0.07 has a pixel pitch of $20 \times 20\mu m^2$ and a total active area of $1.280 \times 5.120\text{mm}^2$. The length L of the internal gate has been reduced by a changed deep n-implantation. A modest reduction from the standard length of $L = 5\mu m$ to $L = 4\mu m$ will be proven to have an impact on the internal gain g_q as high as 80%. The label of this module will be "HiG" in following.

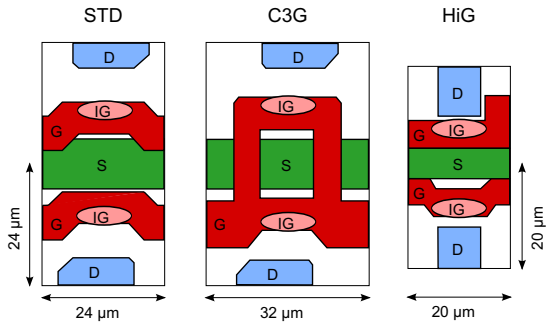

(a) Metallization contact layer.

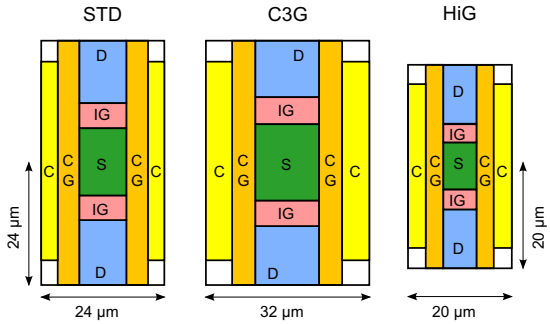

(b) Implantation zones.

Figure 4.2: Layout of the metallization layer (a) and the implantation zones (b) of the double-pixel structures. Shown are the source (S), gate (G) and drain (D) contacts of the FET structure as well as the approximate position of the internal gate (IG). The metal contacts of the clear region (C) and clear gate (CG) are not shown.

5 Preprocessing

The output of the data acquisition (DAQ) are full frame non-zero-suppressed and non-noise-rejected data, which allows detailed studies on the full data level. On the other hand, the full information makes extensive offline analysis necessary. In this chapter, the composition of the signal as well as the offline analysis steps will be discussed and the software framework, in which this analysis is preformed, will be presented.

5.1 ILC - Analysis Framework

For the analysis of the DEPFET data, the ILC-software framework *Marlin* [Mar10, GBGJ03] and the processor compilation *EUTelescope* have been adapted and used. Marlin stands for Modular Analysis and Reconstruction for the LINear collider and was designed to simplify data processing and analyzing. Processors are subroutines written in C++ that perform the data extraction or manipulation. Basic input-output handling can be left to the framework and is controlled through callbacks in the processors. Which Marlin processors will be used, their order and parameters are defined in an XML (Extensible Markup Language) file, which steers the analysis or data manipulation. The EUTelescope analysis package is a Marlin processor compilation that has been developed within the EUDET project to facilitate the offline analysis of sensor prototypes in beam test studies [B$^+$07b]. This compilation offers all tools necessary to derive complex track objects from raw data. The sensor design and readout used were not identical to the EUDET telescope devices, and a handful of modifications and additions were implemented[1]. However, it proved to be a good basis for a detailed DEPFET prototype analysis.

In this chapter, all steps in the analysis chain will be laid out and relevant processors, their function, and parameters are described. A flowchart of the data processing chain is shown in figure F.1 in appendix F.

[1]The modifications and additions are summerized in appendix C.

5.2 Conversion to LCIO Standard

The *LCIO* (Linear Collider Input/Output) standard defines a data model for linear collider detector studies. It is intended to be used in simulation studies and analysis frameworks. Because of its lightweight and portability, it can also be used for detector research and development. *lcio-files* are the standard input output containers of the Marlin framework. The first step in the analysis of the DEPFET data is therefore a conversion of the native DEPFET DAQ output format to the LCIO format.

The *DEPFETReader* processor constructs a run header containing the name of the detector, the run number, the number of detectors, and the amount of pixel in the columns and rows. It further writes for every triggered event an *LC-Event* containing a header with the detector name, the run number, and the trigger number, as well as the *TrackerRawData* collection containing the pixel-wise ADC values for all modules in the setup.

5.3 Pedestal and Noise Calculation

The raw signal is composed of four independent contributions. One of which is the valuable charge signal that carries information about the particles passage through the detector. The first step in the extraction of any information about the interaction of the particle with the detector material must therefore be the extraction of this charge signal from the raw signal. The four contributions to the raw signal are the pedestal value, common mode noise, Gaussian readout noise, and the charge signal

$$S_{ij}^{raw} = S_{ij}^{ped} + S_{i}^{cm} + S_{ij}^{wn} + S_{ij}^{sig}. \tag{5.1}$$

5.3.1 Pedestal

The 14 bit ADC in the S3b board (cf. section 3.3) is tuned, so the pedestal current is sampled to approximately 8000 ADC counts. This leaves room for downward fluctuations and enough dynamic range for sampling signal carrying pixels. The pixel-wise variation of S_{ped} within a sensor are in the order of 10 ADC counts. The time dependence of the pedestal value is studied by comparing the pedestal map (i.e. the pedestal for every pixel) calculated from two runs taken 5 days apart. The pixel-wise difference between these samples is histogramed in figure 5.1 (a). The RMS of the

distribution is approximately 0.8 ADC counts, which corresponds to $\approx 5\%$ of the average noise, thus in the following analysis the pedestal will be taken as constant within a run.

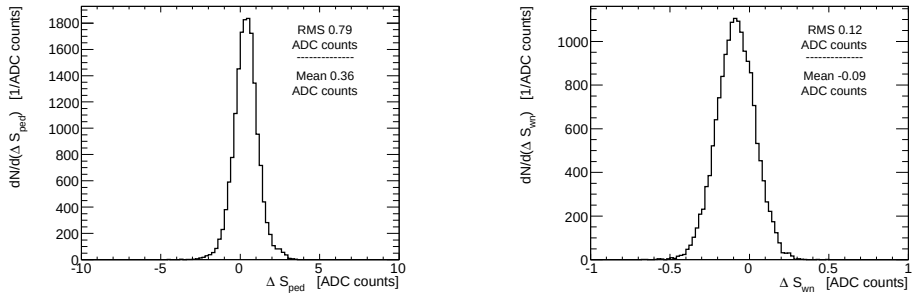

(a) Shift in the pedestal value.

(b) Shift in the noise value.

Figure 5.1: Histogramed pixel-wise difference of condition-files calculated from two runs 5 days apart (run 2169 and run 2291, telescope module Mod 9).

In a sample with no particles passing the detector and in the assumption that the mean of the common mode noise and the white noise is zero, the pedestal value can be estimated as the average of the raw signal

$$\lim_{n\to\infty} \frac{1}{N}\sum^{N} S_{ij}^{raw} = S_{ij}^{ped} + \underbrace{\frac{1}{N}\sum^{N} S_{i}^{cm}}_{=0} + \underbrace{\frac{1}{N}\sum^{N} S_{ij}^{wn}}_{=0} + \underbrace{\frac{1}{N}\sum^{N} S_{ij}^{sig}}_{=0}. \qquad (5.2)$$

In practice, it can not be assured that for a given sample there is no particle passage through the detector. This makes it necessary to reject pixel values from the calculation that contain signal charge. In principle, the identification of these hits depends on the quality of the pedestal estimation. This dilemma is solved by iterating the pedestal and noise calculation.

5.3.2 Common Mode Noise

The common mode noise is a row-wise correlated noise of ≈ 20 ADC counts caused by the row-wise read out of the pixel matrix. Its contribution to the total noise is on the same level as the random noise. Figure 5.3 (c) shows an exemplary common mode distribution. S_{cm} is heavy fluctuating from event to event, but for a given event totally correlated within a half of a double-row, which is caused by the sampling of the left and the right part

of the double-pixel row in separate TIA and DAC (cf. section 3.3). This can be used to estimate the common mode noise of the raw signal. Taking that the mean of the white noise is zero and requiring no charge signal, a possible estimate of the common mode noise is the pedestal subtracted arithmetic mean of the ADC counts of a half double-row

$$\frac{1}{64}\sum_{j=0}^{64}\left\{S_{ij}^{raw}-S_{ij}^{ped}\right\} \approx S_i^{cm} + \underbrace{\frac{1}{64}\sum_{j=0}^{64} S_{ij}^{wn}}_{\approx 0} + \underbrace{\frac{1}{64}\sum_{j=0}^{64} S_{ij}^{sig}}_{=0}. \tag{5.3}$$

As for the pedestal calculation, a proper hit rejection is crucial for the quality of the common mode estimation, and at the same time a good quality in the common mode estimation ensures an efficient hit finding and rejection. To reject hits from the common mode calculation, the median, which is an outlier resistant mean estimator, will be used instead of the arithmetic mean in the following discussion.

5.3.3 Start-Gate Artifacts

Artifacts stemming from the start-gate rows, i.e. the first row read during the read cycle (cf. section 3.3), were noticed after inspection of the common mode noise. Figure 5.3 (a) shows the common mode noise distribution of the STD DUT. The central region shows a Gaussian behavior with a strong deviation in the tails of the distribution and a peculiar accumulation in the high energy region of 1500 to 2000 ADC counts (not shown in the plots). Further the signal of these outliers depends on the physical position of the corrected row as can be seen in Fig. 5.3 (b).

A close inspection of the events that contained a high common mode noise showed a correlation of these rows and the start-gate position. Figure 5.2 displays such an event containing a scintillating double row and a pointer to the start-gate position. This readout artifact is problematic,

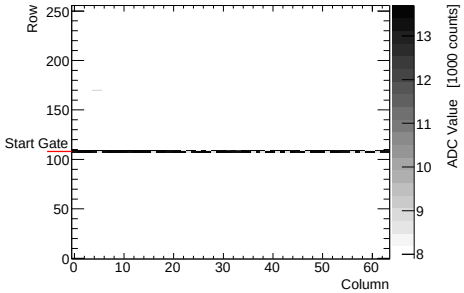

Figure 5.2: Raw data frame with a strong common mode fluctuation in the start gate double row. The common mode noise in the start gate row cannot be corrected without residues. All signals in these rows will therefore be neglected in the analysis.

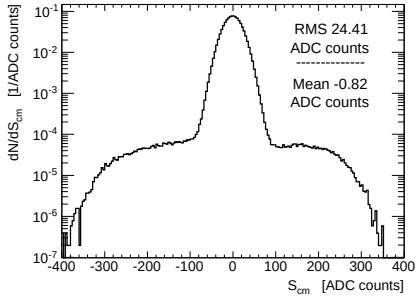

(a) Distribution of S_{cm} before masking of the start gate row.

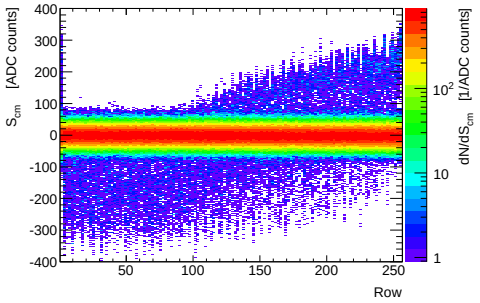

(b) Common mode noise as a function of the sampled row before start gate masking.

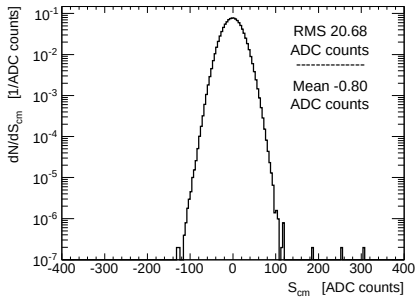

(c) Distribution of S_{cm} after masking of the start gate row.

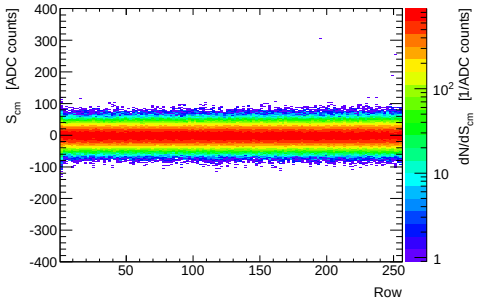

(d) Common mode noise as a function of the sampled row after start gate masking.

Figure 5.3: Common mode noise distributions before and after the masking of the start gate double row. The start gate rows have a higher common mode noise and lead to a deviation from the Gaussian shape observable in the over expressed tails (a). S_{cm} is biased by the position on the matrix (b). After common mode correction both artifacts vanish (c) and (d).

since the fluctuations within a scintillating row after common mode correction are in the range of 100 ADC counts, which is significantly larger than the expected fluctuations due to the Gaussian noise, which are in the order of 10 ADC counts. These fluctuations thus will be identified as signal by the clustering algorithm [2]. The start gate rows are therefore masked during conversion to the lcio-file and neither allowed for pedestal, noise, or status calculation nor for the calibration and clustering procedure.

After the masking of the start gate double row, the common mode noise distribution follows a Gaussian. The high value contributions and

[2]These start-gate artifacts would appear in the low energy region in the straggling function.

the overrepresented tails and the dependence on the sampled row have vanished as show in figure 5.3 (c) and (d). The common mode noise is for all modules on the level of 20 ADC counts.

5.3.4 Leakage Current

The remaining deviation of the common mode distribution from the Gaussian stems from a correlation of the common mode noise with the distance of the sampled row from the start-gate position. This characteristic is a result of the different speeds of the clear and the readout cycle. Figure 5.4 shows this dependence for two different readout sequences with different time consumption for the read cycle. The clear cycle of the sequence utilized for data taking takes $53\mu s$, whereas the readout cycle takes $2.32ms$ per frame. This leads to an increasing signal integration time with the distance to the start-gate and an increased noise through leakage current and light. This phenomenon has been reduced to a minimum by application the fast readout sequence and is unproblematic for further processing.

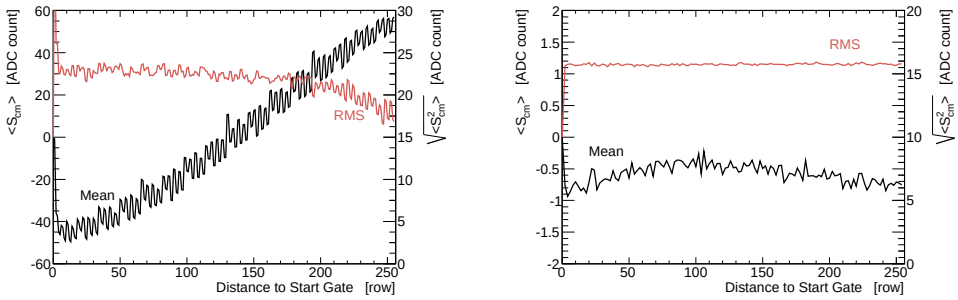

(a) Common mode of an early runs (<2081), which are read out with a slow sequence show dependence on the distance to the start gate.

(b) Employment of a fast readout sequence in later runs (>2088) suppresses the influence of leakage current on the signals.

Figure 5.4: Mean and RMS of the common mode distribution as a function of the distance from the start-gate to the corrected row. All data shown is extracted from telescope module Mod 11 (run 2041 and 2169).

5.3.5 Screen Wiper Effect

The difference in speed of the clear and readout cycle can also be observed in the increased number of clusters that are found with increasing distance

of the cluster to the start-gate. This so-called *screen wiper effect* shown in figure 5.5 is not affecting the performance of the DUT but will have an influence on the telescope reconstruction efficiency in case of a two track event. The first particle triggering the readout will be captured completely. Any particle traversing the telescope during the readout phase may or may not be captured during the readout wipe depending on the particles passage position and the position of the start-gate row.

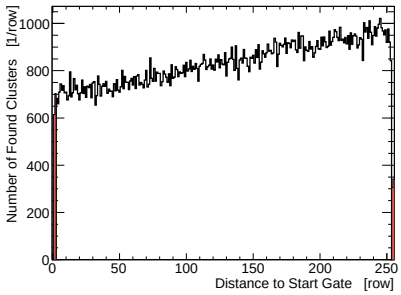

Figure 5.5: Number of clusters versus the distance to the start-gate row. The increased number of clusters with distance to the start-gate is caused by the different timings of clear and read cycle. The red area represents the start-gate clusters excluded from the analysis.

5.3.6 Random Noise

There is no method to remove the fluctuations of the pedestal and common mode corrected raw signal. This random noise S_{wn} of a pixel follows a Gaussian distribution with an RMS value in the range from 10 to 20 ADC counts as can be seen from figure 5.6. The RMS of the noise is used as a delimiter to distinguish signal from noise.

The stability of the Gaussian is in the range of 0.1 ADC counts per 5 days as shown in figure 5.1 (b). The noise level is thus taken as constant within a run.

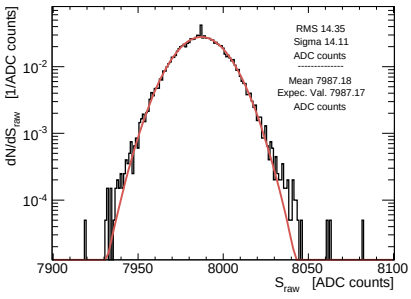

Figure 5.6: Raw signal distribution of a single pixel in STD after common mode correction. The width and expectation value of a fitted Gaussian (red) is in good agreement with the RMS and arithmetic mean of the raw signal distribution (black).

5.3.7 Charge Signal

The charge signal is a measure of the charge collected in the DEPFET internal gate. During the beam test session, the impinging particles were mostly pions at 120 GeV leaving a broadly distributed charge signal in the range of 500 to 1500 ADC counts in a hit pixel. A detailed analysis of the charge signal will be presented in the following chapter.

5.3.8 Calculation of Pedestal and Noise

The pixel-wise pedestal (S_{ped}) and noise (σ) are calculated using the *EUTelPedestalNoiseProcessor*. The pedestal is estimated as the mean and the noise from the RMS of the ADC values from a sufficient large sample of standard events. To reject events in which the pixel carried signal, and which should therefore not be used for pedestal or noise estimation, the calculation is iterated. In all but the first passage, the common mode noise is estimated and subtracted. At the end of the calculation, abnormal pixels can be masked based on their noise and pedestal values.

During the first passage neither mean nor RMS are known. All n_e events of the sample contribute to the calculation. After the first passage, the pedestal and noise is overestimated because high ADC signals from hits are not rejected from the calculation. In addition, the common mode noise further increases the bias of the noise estimation. The first loop estimates the mean and RMS as

$$S_{ped} = 1/n_e \Sigma S_{raw} \tag{5.4}$$

$$S^2_{RMS} = 1/n_e^2 \Sigma S^2_{raw}. \tag{5.5}$$

In the subsequent loops S_{ped} is used to determine the common mode noise, which is then subtracted from the raw pixel value. The common mode noise is calculated as the pedestal corrected median of a half double-row. This algorithm has been chosen because it is insensitive to outliers (i.e. hit pixels) within the sampled row. A common mode corrected value is only considered for the recalculation of pedestal and noise if it is within a 7 σ neighborhood of the pedestal value determined from the first loop [3]. After the second loop the estimation of the pedestal and noise have improved due to the hit rejection. The third loop is similar to the second one but based on refined pedestal and noise estimates. All loops following

[3]The signal-to-noise ratio of the detectors is > 100, which allows the 7 σ cut.

the first one estimate the mean and noise as

$$S_{ped} = 1/n_{w/o}\Sigma\left(S_{raw} - S_{cmc}\right) \tag{5.6}$$

$$S^2_{RMS} = 1/n^2_{w/o}\Sigma\left(S_{raw} - S_{cmc}\right)^2 \tag{5.7}$$

from a signal rejected set of events $n_{w/o}$. The noise of a pixel is calculated after the third loop by

$$\sigma = \sqrt{S^2_{RMS} - S^2_{ped}}. \tag{5.8}$$

To identify dead, noisy, and hot pixels, constraints for a healthy pixel can be defined. These constraints are checked at the end of the last loop. A minimal and a maximal absolute noise value as well as a minimal and maximal pedestal value can be set. Noisy pixels are identified by demanding that the noise has to be within a certain RMS-neighborhood of the noise distribution's mean.

After the masking of abnormal pixel, the noise, pedestal, and status maps are saved as 3 collections in a single event to a *condition-file* in the LCIO format. The reprocessing parameters obtained for the DUT are collected in table 5.1.

DUT	STD	C3G	HiG
Pedestal [ADC counts]	7996 ± 18	8020 ± 29	8212 ± 33
Noise [ADC counts]	13.95 ± 0.30	16.42 ± 0.57	15.22 ± 0.55
number of masked pixel	0	1267	128

Table 5.1: Pre-processing parameters for the DUT. Pedestal and noise are calculated pixel-wise – shown here is the average pedestal and noise as well as the RMS spread of the values. Masked regions are shown in figure 5.16 (b).

5.4 Calibration of Data

With the information from the condition-file, the pedestal and common mode contributions can be subtracted from the raw signal. Once again, the common mode contribution is calculated as the median of a half double-row. This is done in the *EUTelCalibrateEvent* processor. The calibrated ADC values for each event and module are saved to a data collection.

5.5 Fixed Frame Clustering

Clustering is the process of identifying pixels, which carry charge created by the passage of the same one particle in an event. The method of clustering is crucial for the identification and disentanglement of the hits on the sensor and thus for the performance and efficiency of the detector. A simple approach is the fixed frame clustering. In this grouping algorithm, the pixels in an rectangular area around the highest signal that exceeds 5 σ (seed signal) are called the neighbors and form the cluster together with the seed pixel. The pixel of a cluster are marked as hit and will be excluded from the iterated seed search. In the following analysis, a cluster size of 5x5 will be utilized, unless stated otherwise.

The sum of all pixel ADC values of a cluster is called the *cluster signal* and should represent the deposited energy in the detector if all signal is contained within the cluster frame. It is common to constrain the cluster formation by including only neighbors with a signal greater than 2.6× noise [K$^+$09]. Although by this means the resolution of the device can be improved, as will be shown in section 5.6.4, the neighbor cut will not be employed in the following discussion to avoid the introduction of a systematic bias and the resulting underestimation of the cluster signal.

Four flags can be used to indicate the qualities of a cluster:

- The quality flag of a cluster is set to *incomplete* if it contains a pixel that has been masked as dead or hot in the pre-processing or if the pixel has already been added to another cluster.
- It is marked as *merged* if it has been found close to another cluster and charge sharing can not be ruled out.
- If the cluster is found not to be fully contained within the pixelated area, it is of the *border* type.
- If the cluster frame contains pixel that were set to zero during the masking of the start-gate, the flag *start-gate* is assigned.

This algorithm performs well at low occupancies and with prior knowledge about the expected typical cluster size. The major drawback of this algorithm is the inability to deal with δ-ray events that produce knock-on electrons that carry signal charge past the cluster border. As shown in section 2.3 in 8% of the events a δ-ray with an energy large enough ($> 100keV$) to travel past the cluster boundery ($> 50\mu m$) is produced.

DUT	STD	C3G	HiG
Total	231702	196316	73017
Good	180828 78.0%	70421 35.9%	53220 72.8%
Incomplete	14728 6.4% / 0.1%	85038 43.3% / 0.1%	7481 10.3% / 0.1%
Border	16496 7.1% / 7.7%	20075 10.2% / 7.7%	4824 6.6% / 7.7%
Merged	33046 14.3% / 1.1%	101093 51.5% / 1.3%	14058 19.3% / 0.6%
Start-Gate	2727 1.2% / 2.4%	3495 1.8% / 2.4%	917 1.3% / 2.4%

Table 5.2: Quality flags assigned in the runs 2169 (STD), 2266 (C3G), and 2185 (HiG). The large numbers represent the amount of events found with the corresponding flag. The percent values are the measured and expected (M/E) fractions.

This signal leakage from the primary cluster may lead to the formation of a secondary cluster (cf. section 6.2). These events can be identified with the *ClusterSeparation* Processor that flags two clusters as *merged* if the distance between their seeds is smaller than 7.22 pixels. The probability that the clusters of two real particles that traverse the device are positioned less than d pixel apart can be estimated under the assumption of uniform illumination via

$$\rho = \pi d^2/(256 \cdot 64)\text{px}. \tag{5.9}$$

The value of $d = 7.22$ pixel has been chosen to limit this probability to 1%.

5.5.1 Quality Flags

In table 5.2 the absolute number and relative fraction of clusters attributed to the different quality classes as well as the expected values are shown for three runs containing the different DUT. In the following listing, a qualitative discussion on the probability of the different cases as well as an explanation for deviations is given.

- The frequency of the *incomplete* clusters on STD and HiG is on the percent level and mainly caused by formation of secondary clusters

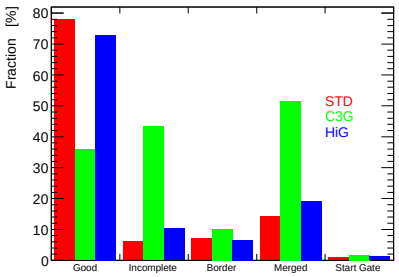

Figure 5.7: Fractions of quality flags assigned to clusters found on the DUT. The fraction of merged and incomplete clusters is higher than expected due to signal leaking out of the fixed frame. The number of clusters involving pixel that lay within the start-gate or border region match the expectations.

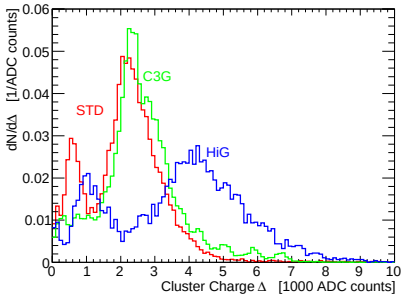

Figure 5.8: Cluster signal distribution of the merged type clusters. The two peak structure is the result from incorrect dissociation of a single hit into two or more clusters.

around charge leaks that share pixel with the primary clusters. The large fraction of *incomplete* clusters on the C3G is caused by the 1267 pixel masked as bad.

- The clusters marked as *merged* include all clusters whose distance is less than 7.22 pixel to another cluster. The expectation for the *merged* cluster frequency can be calculated using the cluster occupancy. The probability that the distance between two clusters in an event with exactly two clusters is below the threshold can be estimated as the fraction of the cluster area to the total active sensor area. In the present case, the threshold is chosen so that the probability is one percent. A first order estimate of the total frequency P is given by

$$P = \sum_{i=1}^{n} \left(\frac{1}{2} i^2 - i \right) \cdot o(i) \cdot 1\%. \tag{5.10}$$

with the probability for an event with i hits $o(i)$.

The fraction of clusters (cf. figure 5.7) is significantly larger than the expected values which are in the range from 0.6 to 1.3 percent. This leads to the assumption that the over-representation of clusters in close proximity is not only caused by independent particles but stem from the same particle. In these hits the ionization charge leaked out of the primary cluster frame and a second cluster has

been formed. This assumption is further supported by the charge distribution of the merged type clusters shown in figure 5.8 where two peaks are observed. The high energy peak at 2000 ADC counts stems from the primary cluster and the low charge peak at 500 ADC counts stems from the secondary cluster formed around the leaked charge. Especially clusters with a high charge deposition leak out of the fixed 5x5 frame as can be seen from the shift of the most probable value (MPV) of the cluster signal distribution in figure 6.2 of $\approx$ 3000 ADC counts to $\approx$ 4000 ADC counts (for HiG) found in figure 5.8.

- The clusters marked as *border* type for STD and HiG have a frequency slightly below 7.7% which would be the expected occupancy if the cluster position would be uniformly distributed across the matrix. The deviation stems from the Gaussian beam profile that leads to more clusters towards the center of the matrix. The *border* type clusters on module C3G contribute to a larger fraction since it contains more masked pixels in the center than in the border region and because a noisy column in the border frequently produces noise clusters.

- The expected fraction of *start-gate* type clusters is 2.4 percent. The observed frequency is in the range of 1.2 to 1.8 percent. This deviation stems from a reduced probability to find a cluster adjacent to the start-gate row (cf. figure 5.5).

5.5.2 Occupancy

The occupancy n is the number of particles that passed through the detector and left their foot print in the data frame. Figure 5.9 shows the occupancies of three runs with the DUT in the beam.

5.6 Position-Finding Algorithms

The position-finding is the construction of a space point on the particles trajectory from cluster position, cluster signal, and sensor geometry. The z position, which is parallel to the beam axis, is given by the geometry description of the telescope setup and has been measured with a ruler (cf. figure 4.1). x and y positions are extracted from the sensor signals.

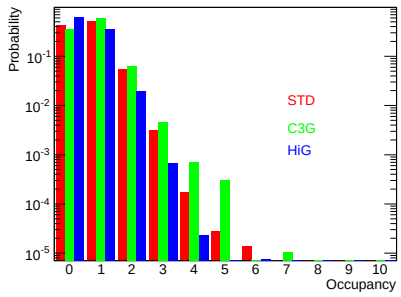

Figure 5.9: Occupancy distribution of the three standard runs containing the DUT: 2169 (STD), 2266 (C3G) and 2285 (HiG). A exponential behavior is expected and can be observed in the runs 2266 and 2285. The run 2169 deviates in the high occupancy tail from the exponential. The average occupancies for are 0.64 (run 2169), 0.73 (run 2266) and 0.40 (run 2285).

5.6.1 Drift of Ionization Charge

The electrons created in the silicon bulk by an impinging particle are drifted through an external electric field towards the internal gates of the DEPFET sensor. The electric field in the bulk is dominated by the potential of the backside electrode creating the sideward depletion (cf. section 3.2.2). The resulting field is laterally uniform and approximately proportional to the distance to the front side [Koh08]. This results in a solely diffusive lateral electron movement and a directed pull towards the front side. However, in the proximity of the front side surface, the static charge of the deep n-implantation exerts a lateral force to the drifting charge separating and collecting the signal electrons in the lateral structure of the internal gates. In the following discussion, the term *surface charge distribution* will be used for the two dimensional scalar field representing the signal charge collected in a hypothetical layer parallel to the surface after the drift though external field and neglecting the subsequent lateral separation (cf. figure 5.10) it will be denoted as $\xi(x)$.

After a particles passage, the signal charge is collected in a cluster of pixels with the seed pixel containing the largest signal fraction. The charge sharing between seed and neighbor pixels depends on properties of the sensor like the carrier mobility, dopant concentration, external field, thickness, and pixel pitch P (i.e. distance between internal gates), and, on the other hand, on the lateral position of the projectiles passage r. The latter dependence is used to refine the estimation of the position reconstruction far beyond the binary resolution of $P/\sqrt{12}$ [Gru93]. In general, the choice of the position-finding algorithm (PFA) depends on charge sharing, incidence angle, and on the possibility to iterate the hit reconstruction.

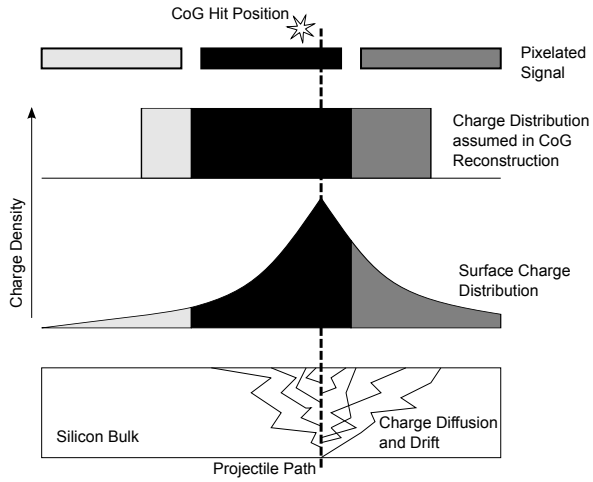

Figure 5.10: Working principle of a position-finding algorithm using the example of the center-of-gravity approach. A projectile penetrates the detector and creates charge. The charge is drifted to the detector surface. The surface charge distribution is registered in discrete pixels and a position is calculated from the pixel signals. The CoG algorithm does not account for the non linearity of the charge sharing and reconstructs the hit with a systematic bias towards the center of the seed pixel.

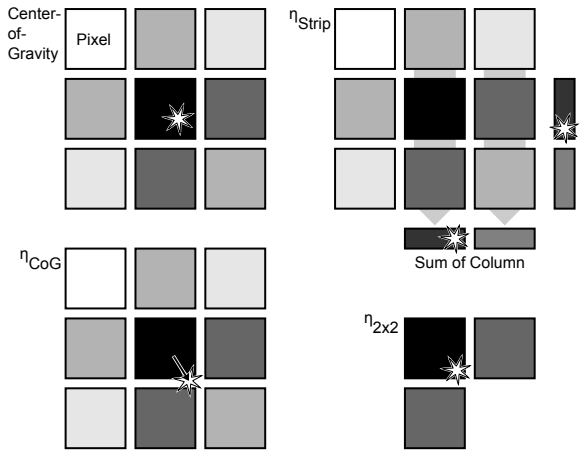

Figure 5.11: Schematic representation of four PFA. The CoG algorithms systematic bias is corrected in the η_{CoG} as indicated with the gray arrow. η_{Strip} combines pixel columns (rows) considering only the two highest strips whereas η_{2x2} considers the two highest pixel signals in the seed row (column) to estimate the point of passage.

5.6.2 Center-of-Gravity PFA

The center-of-gravity algorithm (CoG) is a simple PFA which averages the signal weighted positions of the cluster pixels. The hit position is estimated by

$$r = \frac{1}{\Sigma S_{ij}} \Sigma r_{ij} S_{ij}^{sig} \tag{5.11}$$

with Σ summing up over all signals S_{ij}^{sig} and pixel positions r_{ij} which are part of the cluster.

This algorithm would perform perfectly in the case of a rectangular surface distribution with an average signal density inside the rectangle and zero outside. Its performance decreases with $\xi(x)$ deviating from the rectangular shape. The surface charge distribution and the systematic error introduced by the CoG PFA are illustrated in figure 5.10. In practice, this algorithm may be used before alignment due to its robust working or in the case of a cluster that extends a size of two pixels in each direction. In the following analysis, it will be used for the reconstruction of hits on tilted modules with large cluster sizes and for benchmarking other algorithms.

5.6.3 η Algorithm

In the case of the sensor plane being orthogonal to the beam axis, the cluster size seldom exceeds a width of three pixels. Furthermore, charge sharing is large enough and very few binary hits, i.e. clusters with cluster size equal to one, are found (cf. figure 6.6). This is the perfect scenario for the utilization of the eta algorithm [B+83].

Assuming that a particle uniformly ionizes the sensor material along its path, then the knowledge of the shape of the surface charge density reduces the x (and y accordingly) position-finding to the determination of two parameters. The height of the distribution will depend on the total signal and the position of the peak will depend on the point of passage. Ideally, an algorithm should estimate these parameters from the two pixel with the highest signal to noise ratio. The 2x2 η algorithm relies on the seed pixel (S_S) and the neighbor with the highest signal (S_N). The sum of these signals is a measure of the total charge and the ratio between a measure of the charge sharing. The η-value is defined as a normalized fraction by

$$\eta_{2x2} = \begin{cases} -\frac{S_N}{S_N+S_S} & \text{if } S_N \text{ to the left} \\ \frac{S_N}{S_N+S_S} & \text{if } S_N \text{ to the right} \end{cases}. \tag{5.12}$$

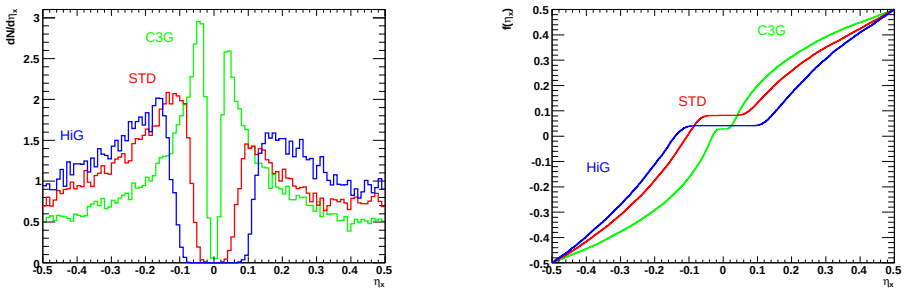

(a) Eta probability density.

(b) Eta distribution function.

Figure 5.12: Eta probability density function and cumulative distribution function.

The η value is projected to the a position within the seed pixel m or a hit position on the sensor r by

$$m(\eta) = Pf(\eta) \tag{5.13}$$

$$r(\eta) = r_S + m(\eta) \tag{5.14}$$

where $f(\eta)$ is a monotonic growing function of η, with $f(-0.5) = -0.5$ and $f(0.5) = 0.5$, P is the pixel pitch, and r_S is the position of the seed pixel.

The $f(\eta)$ is closely connected to the $\xi(x)$ as will be shown further down. One can either derive it from a model or extract it from the experiment. The latter is the standard procedure which returns the most precise hit positions and will therefore be used in the detailed analysis in the following chapter. Under the assumption of uniformly illuminated pixels $f(\eta)$ is given as the integral of the probability density of the η value $\rho(\eta)$ by

$$f(\eta) = \int_{-0.5}^{\eta} \rho(\eta')d\eta' - 0.5 \tag{5.15}$$

The calculation of $f(\eta)$ from preselected high quality clusters (cf. table 5.3) is done in the *EUTelCalculateEta* processor, which writes a lookup table to a condition-file. Figure 5.12 shows the eta distribution $dN/d\eta$ and the integral $f(\eta)$ for the three DUT.

Variations of PFA

In addition to the PFA explained above, modifications of the CoG and of the 2x2 η algorithm are studied. Both rely on equation 5.15 to account for

the non-linearity of the charge density. If equation 5.12 is replaced with the center-of-gravity value

$$\eta_{CoG} = \frac{1}{\Sigma S_{ij}} \Sigma \left(r_S - r_{ij} S_{ij}^{sig} \right) \tag{5.16}$$

the position estimation using equation 5.15 can be improved over the linear CoG PFA.

To determine the one-dimensional hit position, the signals of a pixel column (or rows accordingly) can be added up to form an artificial micro strip detector. The two strips with the highest signal are then used to calculate the η value (equation 5.12) and the position (5.15). This PFA will be denoted η_{Strip}. All four PFA are schematically drawn in figure 5.11.

Measuring the Charge Distribution

The probability density $\rho(\eta)$ can be used to extract the $\xi(x)$ within the boundaries of the seed pixel. Assuming the point of passage is to the left of the center of the seed pixel, then η is connected to $\xi(x)$ by

$$\eta(m) = \frac{-S_N}{S_N + S_S} = -\int_m^{\infty} \xi(x)dx / \int_{-\infty}^{+\infty} \xi(x)dx. \tag{5.17}$$

Setting $\int_{-\infty}^{+\infty} \xi(x)$ to unity and $\xi(\pm\infty) = 0$ the derivative of $\eta(m)$ with respect to m is given by

$$\frac{d\eta(m)}{dm} = \xi(m). \tag{5.18}$$

Extending $\rho(\eta)$ and assuming a uniform distribution of N_0 particles within the interval P returns:

$$\rho(\eta) = \frac{dN}{d\eta}\frac{P}{N_0} = \left(\frac{P}{N_0}\frac{dN}{dm}\right)\frac{dm}{d\eta(m)} = \frac{1}{f(m)}. \tag{5.19}$$

Using of equation 5.15, η can be mapped to m and $\xi(m)$ can be obtained from equation 5.19.

The surface charge distributions calculated in this manner are shown and discussed in section 6.7.

5.6.4 Performance of Position-Finding Algorithms

The performance of the hit reconstruction has been studied by comparing fixed frame clustering with different frame sizes and neighbor cuts and position-finding with different PFA.

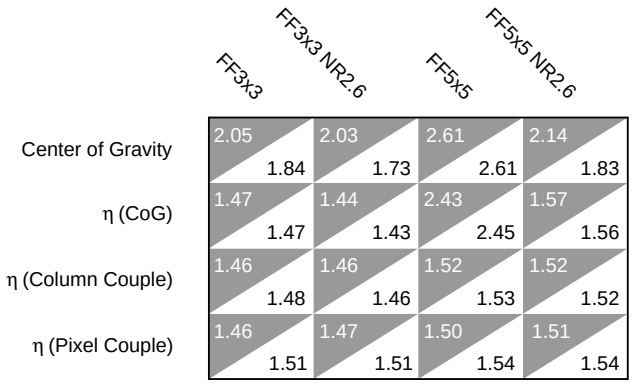

Figure 5.13: Residuals in x and y direction after hit reconstruction with different clustering methods and position-finding algorithms. Clustering is done with the fixed frame size of 3x3 and 5x5 pixel. NR2.6 denotes the rejection of signals that are below 2.6 $\times$ noise. The PFA are explained in the text. The white number on gray ground is representing the residual in x direction and the black on white number the residual in y. All numbers are in units of μm.

Figure 5.13 collects the residuals (a measure of the sensors spatial resolution) for 16 different combinations of clustering and PFA. The studied cluster frame sizes are 3x3 and 5x5 pixel. Clustering is done including and rejecting pixels with signal lower than 2.6 $\times$ their noise. The PFA compared have been discussed in the previous paragraphs and include the CoG, η_{CoG}, η_{Strip}, and the η_{2x2} algorithms.

The systematic bias of the Center-of-Gravity position towards the center of the pixel becomes apparent in the residual values. For a given clustering method it is approximately 25% worse than any of the methods accounting for non-linearities according to equation 5.15. The best residual is achieved with the η_{CoG} PFA in combination with the noise rejected 3x3 clustering. In the detailed analysis of the DUT in the following chapter, however, the 5x5 clustering without the noise rejection will be used. This is motivated by the systematic underestimation of the total signal after noise suppression and signal leakage due to a undersized cluster frame. The best performing PFA with this clustering is the η_{2x2} algorithm, which will therefore be used in the following discussion if not stated otherwise.

5.7 Alignment

To determine the spatial resolution of the DUT, the particle trajectory has to be estimated from the 5 telescope modules that are arranged around the DUT as shown in section 4.2. For an accurate reconstruction of the trajectory, the sensors have to refer to the same coordinate system. This transformation to a common frame of reference is called alignment. In the following discussion, the alignment is the shift of a module in x and y perpendicular to the beam axis z and a rotation around z. These alignment constants (x_{align}, y_{align}, and φ) are calculated via a global χ^2 minimization of a straight line fit through the hits, calculated with the use of the η_{2x2} algorithm, on the telescope planes as well as through the DUT. The alignment constants are determined using the *EUTelMille* processor, which calls the global χ^2-fitter *MillepedeII* [Blo06]. The alignment transformation of the hits positions is applied by the *ApplyAlignment* processor.

To use only clusters with a high probability of belonging to a track that can be properly reconstructed, a pre-selection is performed. The selection cuts can be taken from table 5.3 and include quality, signal, and occupancy cuts to reduce combinatoric effects and apply to the telescope as well as to the DUT. The signal cuts have been derived from the seed and cluster signal histograms (figures 6.1 and 6.2. Further, a region of interest cut (ROI) is applied. This cut is necessary due to biased reconstruction in the border regions of the sensor. This so-called edge effect will be a point of discussion in the following chapter.

The telescope modules as well as the DUT are mounted on xy-tables that have a finite rigidity. This causes the detector modules to move several microns over the course of a run. These movements have to be compensated by repeated alignment. On the other hand, with the number of alignments per run, the accuracy of each alignment drops due to the reduced statistics. The optimal repetition rate will be a trade-off between frequency and sample size. Good results have been archived with a realignment of the telescope and DUT after 10,000 events. To give an example, the relative rolling alignment constants for the run 2169 are shown in figure 5.14.

The alignment algorithm has been cross checked with a Monte Carlo simulation and the use of the DEPFET model described in chapter 7. The simulation confirms the expected precision of $\Delta x_{align} = \Delta y_{align} \approx 0.24 \mu m$ and $\Delta\varphi \approx 0.15 mrad$ for a sample size of 10,000 events (equivalent to $\approx$ 1000 high quality tracks).

	High Quality	Std. Quality
Seed S/N	–	7
Cluster TEL	1000	–
Cluster STD	1000	–
Cluster C3G	1700	–
Cluster HiG	2000	–
Occupancy	1	–
ROI col	$16 < i < 48$	–
ROI row	$16 < j < 240$	–

Table 5.3: Cuts applied for cluster pre-selection. High quality clusters are used for calculation of η and for alignment. The *Seed S/N* cut rejects a cluster if the signal to noise value of the seed is below the threshold. The *Cluster* cut applies to clusters with a total signal below the cut value (in ADC counts). The *Occupancy* cut demands exactly one hit per plane in telescope and DUT. The region of interest (*ROI*) cut is passed by clusters found in column i and row j that lay within the range.

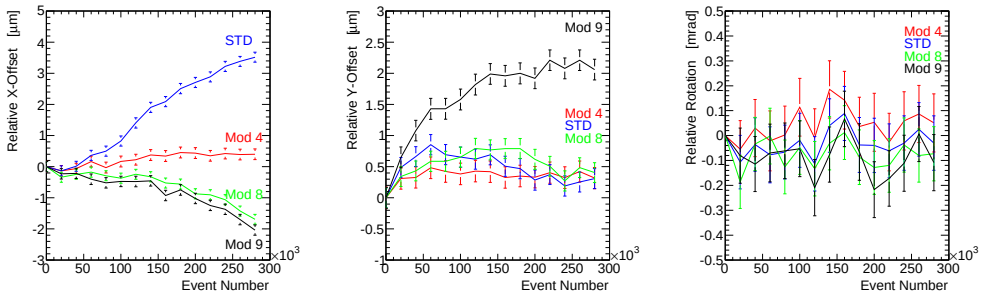

(a) Relative alignment shift in x-direction.

(b) Relative alignment shift in y-direction.

(c) Relative alignment rotation around z-axis.

Figure 5.14: Alignment constants of run 2169 as a function of the event number. The frame of reference is spanned between the first and the last module of the telescope these modules are therefore always at zero and are not displayed.

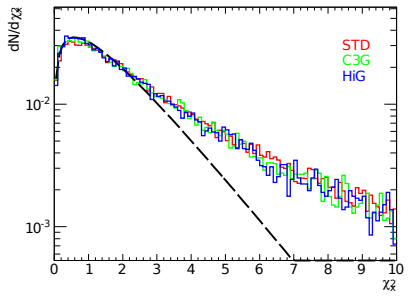

Figure 5.15: χ^2 distribution in x direction from the straight line fit. The dashed line is the theoretical χ^2 distribution for $ndf = 3$ and $\sigma = 1.7$. Deviations in the tail of the distribution stem from the simplicity of the straight line model. Tracks that have undergone scattering deflections cumulate in the high χ^2 regime.

5.8 Tracking

Tracking is the procedure of combining individual hits on the aligned telescope sensor planes to a complex object that describes the particle trajectory. Relating this track to the hit on the DUT provides a measure of the intrinsic resolution of the studied device.

5.8.1 Straight Line Fitting

Neglecting the multiple scattering of the particle on the detector material leads to a straight track. With this approximation and a fixed z position, a track has four parameters, which are the two dimensional space information and the two angles that fix the direction of the track.

The straight line fitting is performed by the *EUTelMultiLineFit*.

For fitting, the track is split into its projections on the x and y plane. *EUTelMultiLineFit* determines the track parameters by minimization of χ^2. This leaves two parameters to be determined from five position values and three degrees of freedom. The χ^2 distributions obtained from the fitting agree with the theory in the low χ^2 regime as displayed in figure 5.15. The cause for the deviation in the tail of the measured distribution from the theoretical is the idealistic assumption of a straight trajectory. The real particle is scattered many times during its passage through the sensor planes and the measured χ^2 tends to higher values.

The distribution of the angle around the x axis and the projected hit position on the DUT are shown in figure 5.16.

The major limitation of this fitting process is the negligence of multiple scattering effects. With rising particle energies and lowering of the sensor material budget, the deviation of the real trajectory from a straight line decreases. In the present case, the straight line approach is a simple and

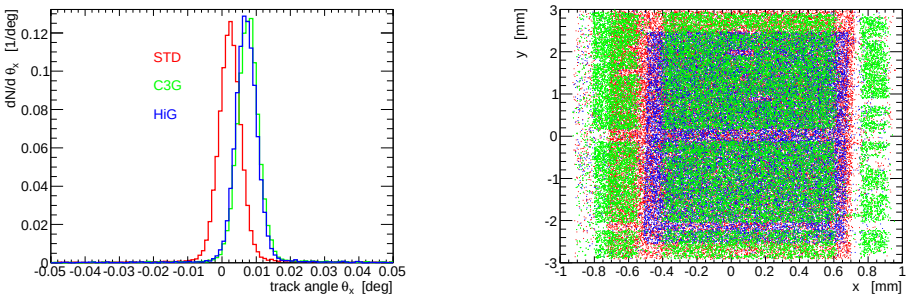

(a) Distribution of the angle around x.

(b) Hit positions on the DUT predicted from the telescope.

Figure 5.16: Parameters of the straight line fit through the telescope modules.

robust approximation with sufficient precision and will be used in the following analysis if not stated otherwise.

5.8.2 Analytical Track Fitting

As shown in section 2.4, the effect of multiple scattering on the particle's position even in a high energy pion beam can be as large as $1.7\mu m$ after the passage through the material of telescope and DUT. An analytical track fitting method following the analytical approach described in [ZN07] is used in the following chapter for advanced tracking. The approach is based on few simplifying assumptions:

- all telescope planes are parallel to each other
- the beam is perpendicular to the telescope planes and has a small angular spread
- particle scattering angles in subsequent telescope layers are also small
- thickness of all material layers are very small compared to the distances between planes
- particle energy losses in telescope layers can be neglected

All of which are fulfilled in the present case.

In contrast to the straight line fit explained in the previous section, the analytical fit allows a bend of the track after the passage of sensor material.

The magnitude of the bend is translated to a contribution to the χ^2 of the track hypothesis according to the Molière theory. The track positions in each detector plane is given by the track hypothesis with the smallest χ^2.

The sensor material causing the multiple scattering is described in the geometry file and includes the $450\mu m$ of sensor silicon and the two $100\mu m$ aluminum windows encasing every sensor.

The analytical track fitting method is called within the *EUTelTestFitter* processor.

6 Analysis Results

Since the start of the DEPFET prototype testing in 2006, beam tests have been performed to gather information about the performance of the sensors and to test DAQ and analysis software. This chapter will present the results of the most recent prototype testing and will rely mainly on the beam test performed in the summer 2009 at CERN SPS.

6.1 Internal Gain – g_q Value

The cluster signal is the sum of all pixel signals included in a cluster and will be denoted S in this section. In contrast to the seed signal, which is the charge deposited in the seed pixel, the cluster signal only depends on the particle's deposited energy and on the amplification of the device. It therefore should be independent of the pixel dimensions.

In the following discussion only clusters that are not marked as *incomplete*, *border*, *merged*, or *start-gate* and whose seed has a signal-to-noise ratio greater than seven are used. The fraction of clusters marked with these different flags has been discussed in section 5.5. These selection criteria suppress incomplete clusters and events from hadronic background and are not biasing the reconstruction.

Comparing characteristic values of the cluster signal distribution shown in figure 6.2 with the corresponding values of the theoretical energy straggling function will reveal the g_q values characterizing the internal gain of the studied prototypes. Two prominent values of the straggling function are the mean $\langle\Delta\rangle$ given by the Bethe theory (cf. section 2.1.1) and the most probable value (MPV) Δ_P derived from numerical calculation by Bichsel (cf. section 2.2.3). The energy deposition in the $450\mu m$ silicon is converted to the number of created electron hole pairs with the W value of $3.6 \pm 0.1eV$ [ICR79]. The mean of the signal $\langle S\rangle$ is calculated from the data sample with the restraint that the seed signal is larger than a threshold derived from the first minimum in the seed signal distribution 6.1. The MVP of the cluster signal S_P is determined from a narrow Gauss fit around the peak of the S distribution. The ADC value is then translated

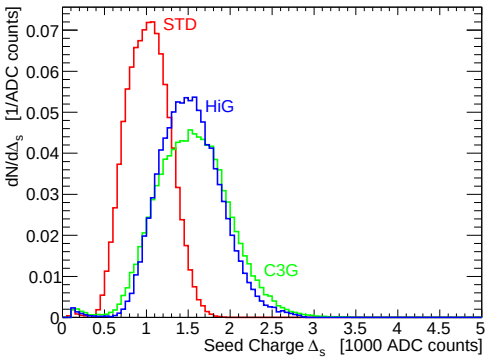

Figure 6.1: Seed signal distribution. The signals increases with gain and larger pixel area. Relative to C3G the pixel of HiG have a 30% increased internal gain but only half the area.

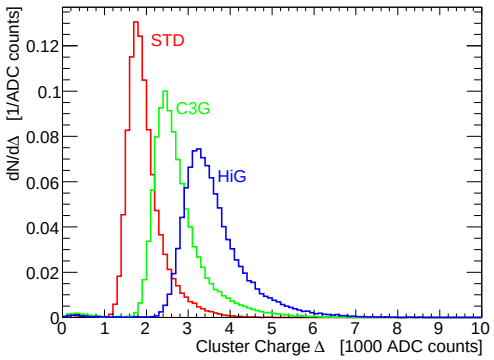

Figure 6.2: Cluster signal distribution. The relative position of the peak is a measure of the matrix internal gain as the ionization charge deposited in the silicon is the same for all devices.

to a current signal by the g_I value of 7660 ± 200pA/ADC count [Koh08] of the readout chain. The number of charge carriers released in the silicon is proportional to the measured current, the connecting factor being the internal gain of the DEPFET device g_q which measures the drain current I_D per electron.

The Bethe theory predicts $\langle\Delta\rangle = 268keV \pm 20\%$. The relatively large error arises from radiative effects which are not included in the theory but have a significant contribution at $\beta\gamma = 857$. A calculation for the radiative loss of muons in iron given in [A$^+$08] has been used to approximate the uncertainty in $\langle\Delta\rangle$. g_q calculated from the mean of the signal given by

$$g_q^{\langle S\rangle} = \frac{\langle S\rangle\, g_I W}{\langle\Delta\rangle}. \tag{6.1}$$

Analogous the gain derived from Bichsel's calculation of Δ_P to $130keV \pm 1\%$ [Bic88] is given by

$$g_q^{S_P} = \frac{S_P g_I W}{\Delta_P}. \tag{6.2}$$

Table 6.1 collects mean and MPV values of the signal distribution as well as the gain values for the three DUT. The discrepancy between the two calculated gain values is apparent and lays within the difficult estimation of $\langle S\rangle$. The internal gain calculated from the MPV $g_q^{S_P}$ is in good agreement with previous measurements using β and γ emitters [A$^+$10a, Esc10] and should be used for referencing.

Three reasons cause the underestimation of the mean $\langle S\rangle$ and the resulting gain value $g_q^{\langle S\rangle}$. (1) The energy deposition in thin silicon is heavily fluctuating with a large tail to high values, i.e. high energy deposits are seldom but contribute significantly to the mean. This leads to a value which is underestimated at start and converges only slowly with increasing sample size. (2) The bigger impact on the deviation is caused by the clustering algorithm. Although the fixed frame clustering is well suited

DUT	Seed Cut	$\langle S\rangle$	S_P	$g_q^{\langle S\rangle}$	$g_g^{S_P}$	S/N
STD	350	1975±5	1791±10	203±41	379±15	128.4±2.8
C3G	550	2767±5	2437±10	284±58	516±21	148.4±5.2
HiG	700	3626±5	3246±10	373±76	688±27	213.3±7.7

Table 6.1: Internal gain and signal-to-noise ratio of the DUT. *Seed Cut*, $\langle S\rangle$ and S_P are measured in ADC counts; $g_q^{\langle S\rangle}$ and $g_g^{S_P}$ in units of nA/e$^-$.

for precise hit reconstruction, it is not able to handle high energy deposits whose signal charge spreads wider than the fixed frame and escapes the primary cluster as discussed in section 5.5. With the exclusion of clusters that are marked *merged*, a bias reducing the frequency of high energy deposits is introduced and leads to the observed underestimation of $\langle S \rangle$ and $g_q^{\langle S \rangle}$. (3) The third effect is the saturation of the internal gate of the seed pixel in the range of 40.000 e^- ($\hat{=}$ 2000ADC counts at STD) which was reported by [Sch08]. Ionization charge above this limit cannot be stored within the internal gate and will thus not contribute to the current signal of the pixel.

The C3G device shows a 36% increase over the g_q value of STD and a 16% increase in S/N. This improvement is caused by the capacitive coupling of the clear gate to the clear contact which allows wider range of operation paramters than the operation in the common clear gate configuration. The device can be tuned to high gain while ensuring a complete sweeping of the internal gate.

The downsizing of the gate length from $5\mu m$ which is the standard length used in telescope modules, STD and C3G to $4\mu m$ found in the HiG module leads to an 81% increase in gain and a 66% increase in S/N in comparison to STD. A strong dependence of g_q on the gate length is expected and discussed in detail in [Rum09].

The signal-to-noise ratio of the devices has been calculated as the fraction S_P/σ [1] (cf. table 6.1) and ranges between 128 and 213. Under the assumption that the noise is predominatly caused by CURO, TIA, and ADC ASIC, the S/N of a thinned device can be estimated by reducing the signal according to the decrease of the active material and leaving the noise unchanged at a level of $\approx$ 15 ADC counts. For a thinned device with a thickness of $75\mu m$ and g_q similar to that of HiG a S/N of 36 can be achieved with the current readout chain.

[1] For the calculation of the S/N of the Belle-type sensors, the cluster signal is used. These devices will have a reduced thickness of $75\mu m$ and a larger pixel pitch. It is assumed that due to these properties most of the signal charge is collected in a single pixel.

6.2 Comparison of Calculated and Measured Energy Straggling

With the help of a Monte Carlo simulation developed by Bichsel [Bic88], the energy straggling $F(\Delta)$ in the $450\mu m$ thick silicon device can be calculated as explained in section 2.2.3. Figure 6.3 shows the calibrated cluster charge spectrum measured with the STD module in comparison to the calculated energy straggling.

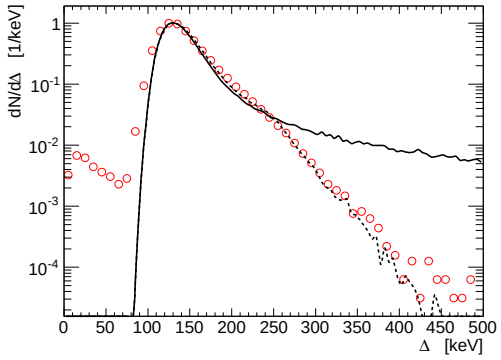

Figure 6.3: Measured energy straggling in DUT STD (circles) in comparison to the calculated $F(\Delta)$ (solid line) and the empirically altered $F'(\Delta)$ (dotted line).

Figure 6.4: Inverted collision spectrum of heavy particles with $\beta\gamma = 1000$. The random number ζ determines the energy loss in a collision $W(\zeta)$ (solid line). Since the high energy transfers play a crucial role for the shape of $F(\Delta)$, the region of $\zeta > 9990$ is sampled with higher precision (dashed line). An ad hoc reduction of these high energy transfers allows a good empirical fit to the measured spectrum (dotted line).

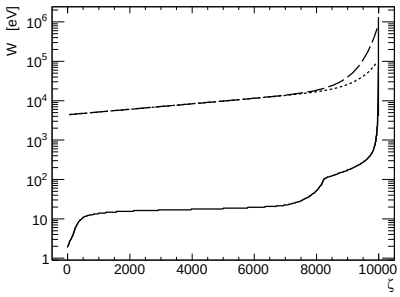

Deviations in the low signal as well the high signal regime are apparent if the data is plotted in logarithmic scale. The overrepresentation of low signal events cannot be explained as the result of the white noise since the probability of a signal to fluctuate above the seed cut of 7σ is 10^{-12}

and the total number of pixel readout is in the order of 10^9. However, low signal could be introduced by δ-rays leaving the primary cluster crossing more than 7 pixel before significantly ionizing the silicon. In section 2.3 the probability of producing a δ-ray that may travel far enough ($> 160\mu m$) to form a secondary low energy cluster is estimated to 4%. Low energy clusters can also be produced by admixtures of high energy particles in the primary beam e.g. muons depositing less energy in the detector.

The reduced number of high energy clusters found can be explained by the inability of the clustering algorithm to deal with δ-electrons. As explained in section 5.5 the fixed frame clustering and the rejection of clusters in close proximity leads to a bias reducing the frequency of high energy deposits. However, a good fit to the experimental data can be obtained with a modest modification of the inverted collision spectrum. One per mille of the energy losses are large ($> 10keV$) and will knock on δ-electrons able to leave the primary cluster. A reduction of these high energy transfers as shown in figure 6.4 representing the reduced energy deposition in the cluster area leads to a good match of the observed and the simulated straggling function and firms the hypotheses of the δ-ray escape.

6.3 Charge Sharing

The magnitude of charge sharing is crucial for the precise reconstruction of the hit position. In the case of a binary hit, the charge sharing did not exceed the neighbor cut and the position can only be reconstructed with an resolution of $P/\sqrt{12}$. With the increase in charge sharing the resolution can be improved. For the optimal hit reconstruction most of the charge created by the impinging particle must be collected in two pixel in each direction. These two pixels should then carry the information about the total amount of deposited energy and through the charge sharing the information about the position of the particles passage. The collection in only two pixels also ensures the highest signal-to-noise ratio possible. With the broadening of the charge sharing the signal-to-noise drops in the two highest signal pixels that are used by the η algorithm [2].

The total cluster size is the number of pixel in a cluster that surpass the 2.6σ threshold. The three DUT studied differ in (1) pixel area, which decreases the average cluster size, and in (2) signal-to-noise ratio (S/N),

[2] A detailed calculation is done in appendix B.

which increases the average cluster size as shown in figure 6.5. The total cluster size will be important for the validation of the Monte Carlo simulations discussed in the following chapter.

The cluster size along the x or y direction of the pixel, which is defined as the maximum x or y distance between two pixel above 2.6 $\times$ noise, is shown in figure 6.6. Like the total cluster size the x and y cluster size increases with gain and decreases with the pitch. The difference between the x and y cluster size of module C3G (figure 6.6 (a) and (b)) shows the impact of the pixel pitch on the distribution as the S/N is constant. Complementary, the difference in the cluster size distributions of the modules STD and C3G seen in figure 6.6 (b) stems only from the difference in S/N since the pitches in y direction are identical.

6.4 Residuals

After clustering, position-finding, and proper alignment the individual hits on the telescope planes can be combined to reconstruct particle trajectories (cf. section 5.8). Relating the individual tracks with the reconstructed hit on the DUT provides a measure of the resolution of the studied sensor. The distance between track projection and hit is called the residual s. In the Gaussian limit the width of the residual distribution Δs equals the resolution of the DUT Δd convoluted with the pointing resolution of the telescope Δt

$$\Delta s = \Delta t \oplus \Delta d. \tag{6.3}$$

6.4.1 Residuals of Straight Track

The residual distribution shown in figure 6.7 relates the hit positions on the DUT to a straight line fitted through the tracking telescope. The

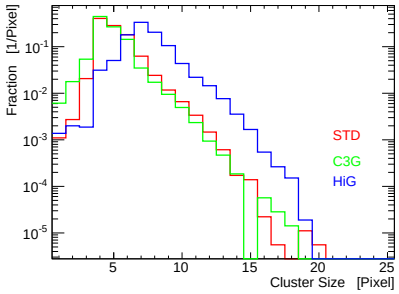

Figure 6.5: Total cluster size distribution of the DUT. The total cluster size is the number of pixel in a cluster that surpass the 2.6 σ threshold.

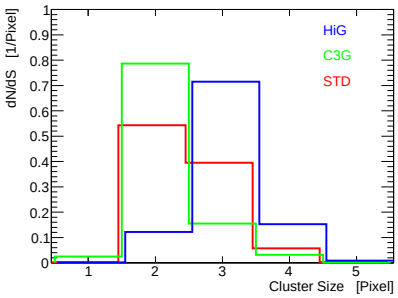

(a) The clusters of C3G are peaking at the optimum width of 2 pixel and the clusters on HiG stretch the widest with a sharp peak at 3 pixel.

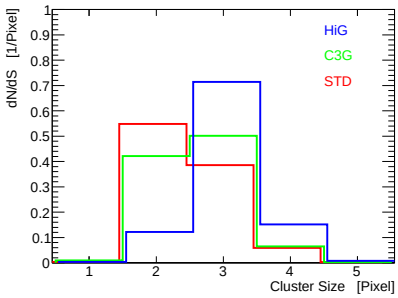

(b) The effect of the increased gain on module C3G is seen in the difference to the distribution of STD since the y-pitch of the two modules is identical.

Figure 6.6: Cluster size distribution in x-direction (a) and y-direction (b).

DUT	dir.	μ	σ	RMS	δ
STD	x	0.01	1.49 ± 0.01	1.96 ± 0.01	1.62 ± 0.01
	y	-0.02	1.54 ± 0.01	1.94 ± 0.01	1.64 ± 0.01
C3G	x	-0.03	1.79 ± 0.02	2.19 ± 0.01	1.92 ± 0.01
	y	0.04	1.65 ± 0.02	1.97 ± 0.01	1.72 ± 0.01
HiG	x	0.01	1.36 ± 0.02	1.61 ± 0.02	1.40 ± 0.02
	y	-0.02	1.50 ± 0.02	1.80 ± 0.02	1.58 ± 0.02

Table 6.2: Results from fitting a Gaussian (μ, σ) to the residual distributions shown in figure 6.7, corresponding RMS values and width of confidence interval δ (CL 68%). All values are in units of μm.

hits are calculated with the η_{2x2} PFA from clusters passing the standard cuts collected in table 5.3 and whose seeds are found within the region of interest. The region of interest cut is applied since the reconstruction and thus the residual in the border region of the device is biased from the edge effect that will be discussed in section 6.8. Table 6.2 collects the results of a narrow (-3 to $+3\mu m$) fit of a Gaussian to the peak of the distributions in x and y direction. The variance σ^2 and mean μ of the fit is a measure of the resolution and a figure of merit for the precision of the alignment. In addition, the RMS of the residual distribution and the width of the confidence interval δ at a level of 68.33% are calculated.

The non-Gaussian tails of the residual distribution can be explained after detailed examination of the η reconstruction process. As will be

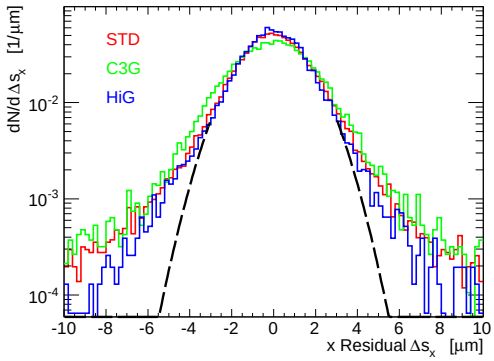

(a) Residuals in x-direction.

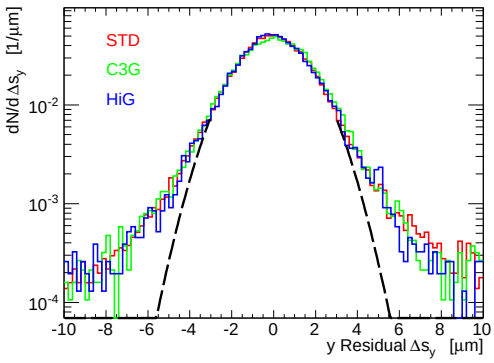

(b) Residuals in y-direction.

Figure 6.7: Residual distributions of the DUT. The hits have been reconstructed from the cluster with the use of the η algorithm. The central region follows a Gaussian, but the tails differ from the expectation (dashed line).

shown in section 6.10 and appendix B, the reconstruction precision of the η algorithm depends on the position of the particles passage with respect to the pixel boundaries. In principle, the reconstruction is best if the particle passes between two pixels and the charge sharing is maximal. Complementary, the worst reconstruction is done if a pixel is hit in the center and the charge sharing is minimal. The intrinsic resolution of the device as well as the residual distribution may therefore not be Gaussian since it represents a combination of the position dependent values.

Also wrong association of hit and track or the reconstruction of a hit position from a clusters produced by δ-rays will result in a huge residual.

Device	dir.	σ	RMS	δ
Mod 11	x	2.11 ± 0.02	2.60 ± 0.02	2.34 ± 0.02
	y	1.95 ± 0.02	2.46 ± 0.02	2.18 ± 0.02
Mod 4	x	1.39 ± 0.02	1.91 ± 0.02	1.52 ± 0.02
	y	1.20 ± 0.02	1.70 ± 0.02	1.28 ± 0.02
HiG	x	1.36 ± 0.02	1.61 ± 0.02	1.40 ± 0.02
	y	1.50 ± 0.02	1.80 ± 0.02	1.58 ± 0.02
Mod 8	x	1.65 ± 0.02	2.05 ± 0.02	1.78 ± 0.02
	y	1.61 ± 0.02	1.97 ± 0.02	1.72 ± 0.02
Mod 9	x	1.80 ± 0.02	2.21 ± 0.02	1.94 ± 0.02
	y	1.90 ± 0.02	2.22 ± 0.02	2.00 ± 0.02
Mod 5	x	2.46 ± 0.02	2.98 ± 0.02	2.78 ± 0.02
	y	2.61 ± 0.02	2.98 ± 0.02	2.82 ± 0.02

Table 6.3: Results from fitting a Gaussian (μ, σ) to the unbiased residual distributions of all sensors, corresponding RMS values and width of confidence interval δ (CL 68%). All values are in units of μm.

6.4.2 Residuals of Analytical Track

The residual distribution shown in figure 6.8 relates the hit positions on the DUT to a track derived form the analytical tracking algorithm described in section 5.8.2. The widths collected in table 6.4 are systematically smaller than the widths obtained with the straight line approach. This is caused by the inclusion of multiple scattering effects into the analytical track fit, which leads to an improvement of the telescope resolution.

6.5 Resolution

The intrinsic resolution is a measure for the error of the position measurement in the detector. With the knowledge of the telescope resolution the spatial resolution of the DUT can be unfolded from the residual distributions, as shown in section 6.5.3.

6.5.1 Upper Limit of Telescope Resolution

To calculate the upper limit of the spatial resolution of the beam telescope the following assumptions are made:

DUT	dir.	μ	σ	RMS	δ
STD	x	0.21	1.29 ± 0.01	1.61 ± 0.01	1.38 ± 0.01
	y	-0.18	1.36 ± 0.01	1.70 ± 0.01	1.44 ± 0.01
C3G	x	-0.59	1.54 ± 0.02	1.89 ± 0.01	1.74 ± 0.01
	y	0.36	1.54 ± 0.02	1.78 ± 0.01	1.62 ± 0.01
HiG	x	-0.10	1.26 ± 0.01	1.49 ± 0.01	1.30 ± 0.01
	y	0.26	1.30 ± 0.02	1.58 ± 0.01	1.36 ± 0.01

Table 6.4: Results from fitting a Gaussian (μ, σ) to the residual distribution of the testfitter shown in figure 6.8, corresponding RMS values and width of confidence interval δ (CL 68%). The uncertainties in σ are calculated in section 6.10. All values are in units of μm.

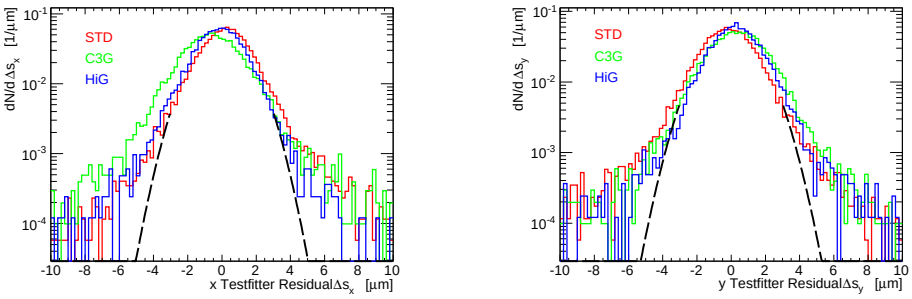

(a) Test-fitter residuals in x-direction.

(b) Test-fitter residuals in y-direction.

Figure 6.8: Distribution of the residual of DUT hit and test-fitter track. The central region follows a Gaussian but the tails differ from the expectation (dashed line).

- all sensor planes are in perfect alignment
- the beam is perpendicular to the sensor planes and has no angular spread
- multiple scattering is negligible
- all sensors are equal and have the same spatial resolution Δx

all of which lead to an overestimation of the telescope resolution.

The unbiased residual s for an arbitrary sensor plane i is given by

$$s_i = x_i - \sum_{j \neq i} x_j / 5 \tag{6.4}$$

with the hit positions x_i. Using the assumption $\forall i : \Delta x_i = \Delta x$ the spread Δs in s can be calculated with Gaussian error propagation by

$$\Delta s^2 = \Delta x^2 + 5 \cdot \Delta x^2 \left(\frac{1}{5}\right)^2 = \frac{6}{5}\Delta x^2. \tag{6.5}$$

Table 6.3 collects the width of the unbiased straight line residuals of all modules in the beam test as determined from fitting of a Gaussian distribution from $-3\mu m$ to $+3\mu m$. The wide spread in the residual widths σ contradicts equation 6.5 and the assumption that all modules are equal. However, the measured values can be used to calculate the upper limit of the telescope resolution. For this purpose the smallest residual spreads in x ($\sigma = 1.36\mu m$) and y ($\sigma = 1.20\mu m$) are picked for Δs. From these values the upper resolution limit of the telescope Δt_u can be obtained

$$\Delta t_u = \sqrt{\frac{1}{5}}\Delta x = \sqrt{\frac{1}{6}}\Delta s_u. \tag{6.6}$$

The corresponding values are calculated to $\Delta t_u = 0.56\mu m$ in x and $\Delta t_u = 0.49\mu m$ in the y direction.

6.5.2 Lower Limit of Telescope Resolution

The position error distribution $D(x', x)$ is the difference between an estimated hit position x' and passage position x. $D(b, x)$ of the binary hit position b, i.e. the center position of the seed pixel, of an ideal detector should be a rectangle centered at zero and with the width equal to the pixel pitch P [Gru93]. For a real detector the sharp flanks of the rectangle

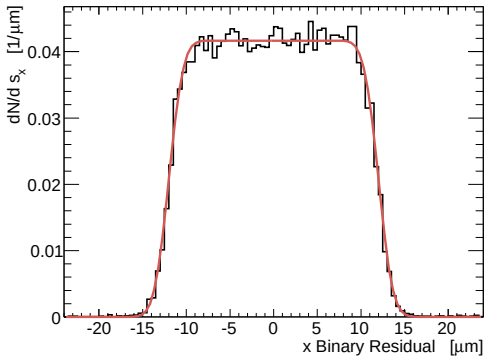

Figure 6.9: Residual of track fit and binary hit position. The smeared edges of the rectangular shape are caused by the limited telescope resolution. Calculated from STD for the x direction. For value of the one parameter (σ of faces) box fit (red line) see text.

are softened by detector noise and emission of δ-rays. In the following these effects are neglected and $D(b, x)$ is assumed to be rectangular which will lead to the underestimation of the telescope resolution and allow the calculation of the lower resolution limit Δt_l.

A measurable variable is the distance between the telescope hit t and the binary hit position b. The corresponding distribution $D(b, t)$ is shown in figure 6.9. This distribution equals the rectangle $D(b, x)$ folded with the Gaussian telescope resolution Δt. It takes the form

$$D(\Delta t) = \frac{1}{P} \cdot \left(erf(\frac{P/2}{\sqrt{2} \cdot \Delta t}) - erf(\frac{-P/2}{\sqrt{2} \cdot \Delta t}) \right). \tag{6.7}$$

with $erf(\frac{P/2}{\sqrt{2} \cdot \Delta t})$ being the error function with the step of width Δt at $P/2$. Fitting equation 6.7 to $D(b, t)$ allows the measurement of the lower telescope resolution to $\Delta t_l = 1.30 \mu m$ in x and $\Delta t_l = 1.29 \mu m$ in the y direction.

6.5.3 Resolution Estimation

The telescope resolution can be estimated from the analysis of the beam test session of 2008 as explained in section 4.2. The resolution of the DUT can be unfolded from the residual distribution Δs with error propagation and using the assumption that the telescope and DUT resolutions are following a Gaussian distribution. Solving equation 6.3 for the DUT

resolution Δd results in

$$\Delta d = \sqrt{\Delta s^2 - \Delta t^2}. \tag{6.8}$$

Plugging the straight line residual widths from the fitted Gaussian (cf. table 6.2) and the estimated telescope resolution ($0.89 \pm 0.22 \mu m$ in x and $0.67 \pm 0.13 \mu m$ in y direction) into this equation results in the resolution estimators Δd collected in table 6.5. From the upper and lower limits of the telescope resolution also the upper Δd_u and lower limit Δd_l in the DUT resolutions are calculated.

DUT	dir.	Δd_l	Δd	Δd_u
STD	x	0.73	1.19 ± 0.16	1.38
	y	0.84	1.39 ± 0.06	1.46
C3G	x	1.23	1.55 ± 0.13	1.70
	y	1.03	1.51 ± 0.06	1.58
HiG	x	0.40	1.03 ± 0.19	1.24
	y	0.77	1.34 ± 0.07	1.42

Table 6.5: Resolution estimates for the DUT. The resolution is calculated for the average, upper and lower limit of telescope sensor resolution. Corresponding residuals are shown in table 6.2. All values are in units of μm.

6.6 Gain Variation

Through the careful analysis of the data from the beam test of 2008 a gain modulation effect on a row-, column- and pixel-wise basis has been observed and studied [Kod10]. In this context one telescope module had a broad variation of g_q in the range of 25% in an row-wise alternating pattern (cf. figure 6.10 (b)). This modulation has a measurable effect on the pointing resolution of the telescope. The impact of the change in gain $g = g_q^1/g_q^2$ of two adjacent pixels on the precision of the hit reconstruction Δx can be estimated from the effect on the center of gravity reconstruction for a two pixel hit by

$$\Delta x = \frac{P S_1 S_2 (1-g)}{(S_1 + S_2)(S_1 + g S_2)} \tag{6.9}$$

with P being the pixel pitch and S_1, S_2 being the measured signals in the pixels. The effect of g increases with charge sharing and peaks at $S_1 = S_2$.

Device	dir.	RMS	RMS_{adj}
STD	x	$2.5\% \pm 0.6\%$	$1.5\% \pm 0.4\%$
	y	$2.2\% \pm 1.5\%$	$1.0\% \pm 1.0\%$
HiG	x	$1.8\% \pm 1.2\%$	$1.6\% \pm 0.8\%$
	y	$3.5\% \pm 3.1\%$	$4.0\% \pm 2.2\%$
C3G	x	$2.6\% \pm 1.0\%$	$1.0\% \pm 0.7\%$
	y	$2.8\% \pm 2.5\%$	$1.7\% \pm 1.8\%$

Table 6.6: Row- and column-wise gain modulation. The RMS value represents the fluctuation in gain in x (from column to column) and in y (gain difference among the rows). The RMS_{adj} represents the fluctuation between two adjacent pixels. All values have been calculated excluding a border region of 16 pixels. The uncertainties have been obtained by bootstraping (cf. section D)

In this case, the gain modulation accounts for a shift of $\Delta x = 1.6\mu m$ for $g = 1.3$ and $P = 24\mu m$.

The pixel-wise gain is calculated from the seed signal. Opposed to the total cluster signal, the seed is not only fluctuating with the charge deposition but additionally with the point of the particles passage, i.e. a central hit will create a higher signal in the seed pixel than a passage between two pixels. Due to theses heavy fluctuations, a large set of hits has to be used for the determination of the pixel-wise gain[3]. A row and column-wise gain modulation can be observed in the test beam data as shown in figure 6.10 (c) and (d). The RMS value of the row- and column-wise gains is a measure for the gain variation and hence for the homogeneity of the matrix. Table 6.6 collects the variations of the gain factor of the DUT. A detailed study using a larger data sample from illumination of the sensors with a β decaying Am-source has been performed by Esch [Esc10]. Esch assumes that the gain variation is caused by the laser used for the deep n^+ implantation which operate in a column-wise pattern.

For the position-finding with the use of the η algorithm only two neighboring pixel signals are utilized. Therefore, only the relative gain difference of these pixels' matters for the proper position reconstruction. The RMS spread of two adjacent pixels is collected in table 6.6. The double-row-wise alternating pattern observed in one module in the 2008 setup significantly influenced this reconstruction and a gain correction has been applied for the determination resolution based characteristics of the de-

[3]For a detailed calculation of the expected uncertainties check appendix D.

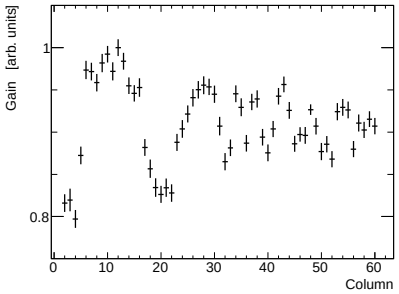

(a) Column-wise gain of module 14B.

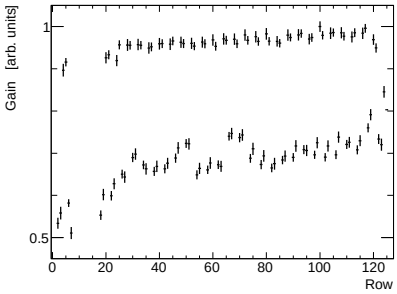

(b) Row-wise gain of module 14B.

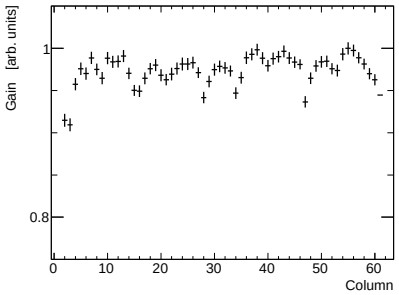

(c) Column-wise gain of module H3.0.11.

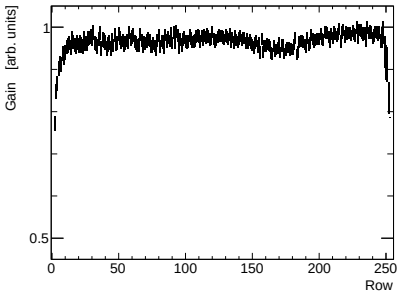

(d) Row-wise gain of module H3.0.11.

Figure 6.10: Gain modulation of abnormal telescope module 14B from the 2008 test beam and of regular performing telescope module H3.0.11 from the test session in 2009. The gain factor has been calculated as the row and column-wise averaged seed signal. The scale is set to unity at the highest value. The complementary graphics for the DUT are shown in figure D.2 in the appendix.

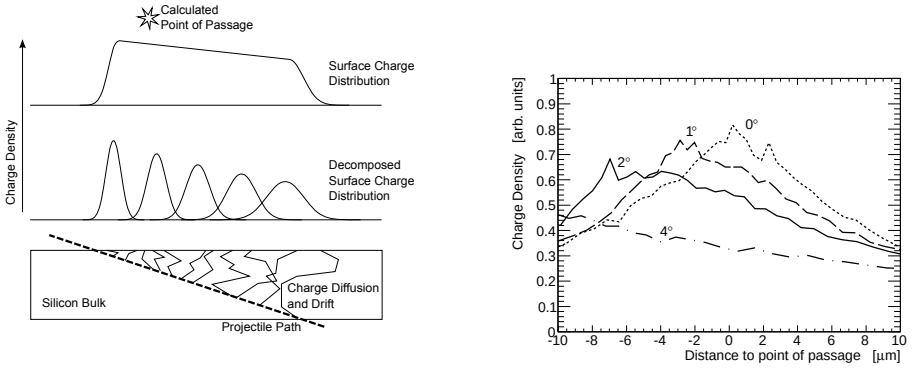

(a) Schematic of the charge collection in a tilted sensor.

(b) Measured charge density for small incidence angles.

Figure 6.11: Schematic of charge deposition and collection in a tilted sensor and measured surface charge densities. The trajectory of the impinging particle has a component parallel to the surface which causes a widening of the charge cloud leading to larger cluster sizes. The dependence of the charge spread on the drift length length causes an asymmetry in the charge density.

vices studies [K$^+$09]. It is, however, not a matter of concern in the evaluation of the data from 2009 since the pixel to pixel difference is in the range of 1% and has no significant influence on the position-finding.

6.7 Angle Scan

During the beam test period of 2008, a set of runs with a tilted DUT have been recorded. The setup of this angle scan is similar to the setup described in chapter 4 with the difference that the DUT could be rotated around the y axis. The projectile trajectories are inclined with respect to the sensor surface and the drift field resulting in a deformation of the surface charge density from its symmetry. The diffusive spread of charge carriers released in the depth of the silicon is wider than the spread of carriers released near the surface. This becomes apparent if the ionization path is tilted since energy deposits near the surface will create a narrow signal on one end of the cluster, whereas the signal charges from the depth will induce a low signal tail on the other end of the cluster. Figure 6.11 (a) sketches this behavior schematically, whereas figure 6.11 (b) shows measured charge densities for different angles.

The cluster size increases with inclination as shown in figure 6.5 and the

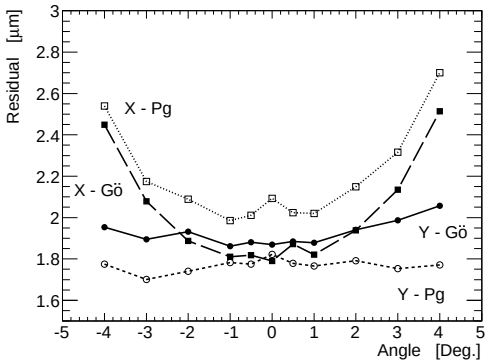

Figure 6.12: Residuals of the DUT in beam test 2008 as a function of the incidence angle of the 120 GeV pion beam. The residuals in x and y are extracted fitting a Gaussian in the limits $\pm 4\mu m$ around the peak of the residual distribution and are marked "Gö". For comparison the results of [K$^+$09] are shown and marked with "Pg". The systematic deviation between the residuals in y are likely to be caused by the application of a gain correction by Kodyš et al. which compensates for the abnormal behavior of module 14B (cf. section 6.6).

performance of the position-finding decreases. The latter aspect is shown in figure 6.12 and compared to the results from [K$^+$09]. The residual in y direction is unaffected by the tilt, whereas the residual in x increases with the angle. This is caused by an increased spread of the signal over more pixels resulting in a decrease in the signal-to-noise ratio in the two pixels utilized for the η_{2x2} PFA. The cluster size in dependence on the incidence angle has been studied in greater detail and will be discussed in section 7.2 of the following chapter.

The differences in the results are caused on the one hand by the application of a correction for the gain variation and on the other hand by the utilization of a 5x5 clustering algorithm with noise rejection by Kodyš et al. This accounts for the superior performance in y as well as for the slight drop of residual in x which is due to an increased frequency of clusters with only one pixel above the neighbor cut of 2.6 $\times$ noise.

6.8 Edge Effect

The response of the detector to a particle passage is not completely homogeneous across the area of the pixel matrix. As shown in figure 6.10 (c) and (d) the seed charge is dropping in the vicinity of the edge of the pix-

elated area and so does the cluster charge. In addition to the incomplete charge collection, a systematic shift of the position-finding is observed in the edge region of the sensor.

The mean of the residual distribution $\langle s \rangle$ of a well aligned detector should be centered around zero and should be independent of the seed position (row i and column j). In the case of a misalignment in x or y the mean should be shifted, but the independence on i and j should hold. Misalignment in the rotation angle ϑ results, for small angles, in a linear dependence of $\langle s \rangle$ on i and j. Figures 6.13 (a) and (b) show a dependence of $\langle s \rangle$ on the column and row of the seed pixel which is not explainable with a merely misaligned detector. A hit registered in the outermost pixels of the sensor is reconstructed with a systematic shift of up to $15\mu m$ towards the sensor border. This edge effect stretches as far as 16 pixel from the border. However, the width of the residual distribution remains nearly constant.

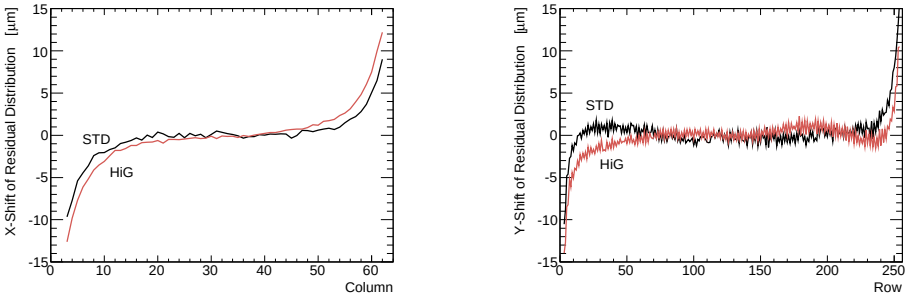

(a) Edge effect in x.

(b) Edge effect in y.

Figure 6.13: Shifted position reconstruction in x and y direction for STD and HiG.

The reconstruction bias can be explained with field distortions near the rim of the matrix. This results in a lateral component of the drift field which drags the ionization charge outwards. To prove this assumption, two additional contacts have been applied alongside the outermost pixel columns of the STD DUT and a set of runs with different voltages applied to this edge contact have been taken. The voltages applied range from 0 to -10 V with respect to the source potential. A schematic representation of the drift field and of the edge contact geometry is shown in figure 6.14. The additional potential should counteract the field distortions and compensate the lateral component of the drift field. Figure 6.15 collects the findings of this scan. A significant effect reducing the shift by $3\mu m$ at

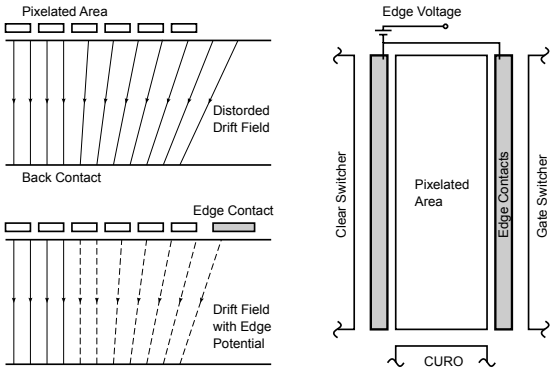

Figure 6.14: Schematic of field distortions in the edge region of the active sensor area and position of edge contacts. Signal charge deposited near the sensor edge is drifted sideways within the electric field (left, top). Applying a negative voltage to the edge contacts placed besides the pixel matrix (right) straightens out the field lines and reduces the lateral drift of the charge (left, bottom). Notice that the sketched field lines only illustrate a general trend and do not accurately represent the drift field.

$-10V$ is apparent only in the x direction which is expected from the edge contact geometry.

The edge effect is biasing the reconstruction on all DEPFET sensors studied so far [K$^+$09]. Since a reliable position reconstruction is only possible in the central region of the sensors, the DUT has been shifted sideways with respect to the telescope modules. This allows a proper reconstruction of tracks in the telescope which penetrate the DUT in the border region. Due to the small area of $1.28 \times 5.12 mm^2$ of the HiG module, which is considerably smaller than the $2.048 \times 6.144 mm^2$ telescope sensors, the edge distortions of this DUT can be studied without moving the device in the telescope. The edge effect on the HiG DUT is shown in figure 6.13 and 6.16.

6.9 Voltage Scan

The voltage applied to the back contact electrode V_{back} of the DEPFET sensor causes the depletion of the silicon bulk and determines the strength of the drift field. A set of runs have been taken with different back contact voltages applied to study the behavior of this important operation parameter.

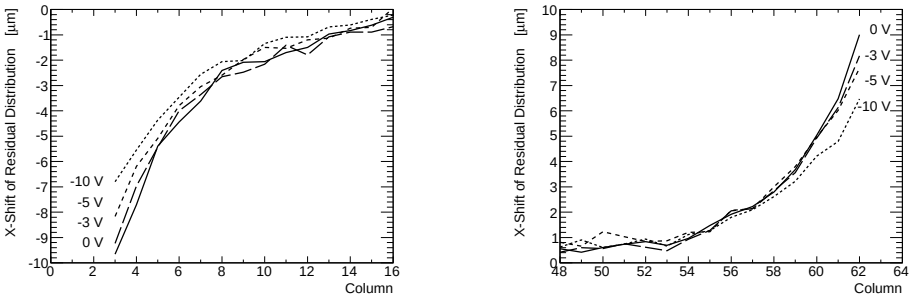

(a) Edge effect in first columns in x.

(b) Edge effect in last columns in x.

Figure 6.15: Effect of different edge ring voltages on systematic shift of position reconstruction on STD DUT.

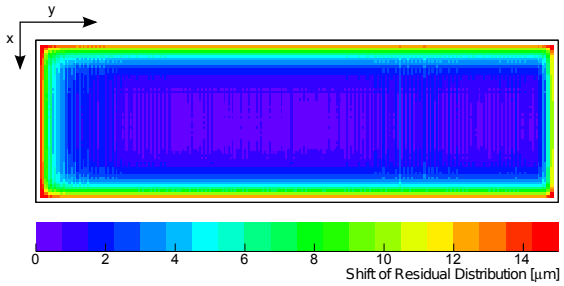

Figure 6.16: Absolute shift of the residual distribution in dependence on the point of passage through the HiG sensor. In the edge region the reconstruction is strongly biased towards the sensor border.

The voltage scan has been performed in the range from -100 to -200 V which includes the normal operation mode at $V_{back} = -180$ V. Figure 6.17 shows the rise of the total cluster charge with V_{back} till a saturation value at $V_{back}^{fd} = -140$ V is reached and the seed signal which increases with V_{back} even beyond V_{back}^{fd}. The rise and saturation of the cluster charge is caused by the growing depletion layer thickness, which is the thickness of the sensitive material, up to the point of full depletion V_{back}^{fd}. The seed signal increase is caused by the increased strength of the drift field and the associated reduction of drift time and diffusive spread resulting in a narrower surface charge distribution.

Under the assumption that V_{back} is much greater than the voltage applied to the front terminal and thus reducing the sideward depleted sensor to a pn diode V_{back}^{fd} only depends on the sensor thickness d and the substrate doping N_D, and is given by

$$V_{back}^{fd} = \frac{qN_D d^2}{2\epsilon_0 \epsilon_{Si}} \tag{6.10}$$

with the dielectric constant for silicon $\epsilon_{Si} = 11.9$. From equation 6.10 the

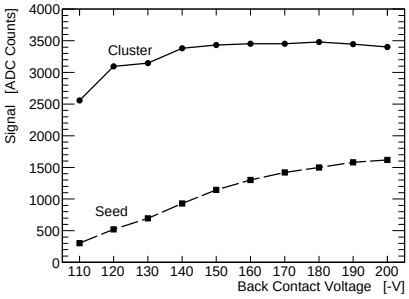

Figure 6.17: Cluster and seed signal as a function of the back contact potential. The cluster signal saturates at full depletion while the seed signal increases with the tighter pull and reduced diffusive spread.

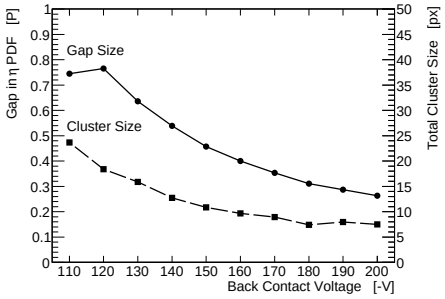

Figure 6.18: Cluster size and gap width of the eta distribution in dependence on the back contact voltage. Both values decrease with the strength of the drift field as diffusive spread is reduced.

doping of the n-bulk can be estimated to $N_D = 6.2$ dopant atoms per μm^3.

The narrowing of the surface charge distribution is also observable in the reduction of the total cluster size with V_{back} shown in figure 6.18. The width of the surface charge distribution further dominates the probability to find a η value close to zero. According to equation 5.12 a η value close to zero can only be measured if most of the induced signal is contained in the seed pixel. The widening of the charge distribution lowers this likelihood and increases the width of the gap in the central region of $\rho(\eta)$. The width of the gap of the η distribution, i.e. the space between the points of half maximum value of the two flanks, in comparison to the total cluster size is shown in figure 6.18. This method of getting a grasp on the width of the charge spread offers the advantage that it is, in contrast to the total cluster size, not dependent on the noise of the sensor nor on a neighbor cut. The shape of the η distribution will be used in the following chapter to validate the digitizer.

6.10 In-Pixel Scan

For the analysis presented here, a total of 1.3 million tracks have been reconstructed from the data taken 2009. Although this represents only an eigth of the 1.8 terabytes collected during the test beam session, the number of tracks is large enough to perform an analysis of the devices

response in dependence on the hit position on the micrometer scale which allows the study of in-pixel properties.

Since the DUT changed during the beam test session and different scans have been performed on the DUT, the full statistic is only available for the analysis of the telescope modules. The limited statistics for the DUT is accounted for in the estimation of the uncertainties and will soften the statements about the charge collection efficiency.

From the hits on all telescope planes excluding the plane to be analyzed, a track is reconstructed. The projection of the track yields an exact measure of the particles passage thought the studied plane. Under the assumption that all pixels are identical, the point of passage $\vec{x}$ can be mapped from the global coordinate system to an in-pixel hit position $\vec{m}$ according to

$$\begin{pmatrix} m_x \\ m_y \end{pmatrix} = \begin{pmatrix} \cos\varphi & \sin\varphi \\ -\sin\varphi & \cos\varphi \end{pmatrix} \left(\begin{pmatrix} x \\ y \end{pmatrix} - \begin{pmatrix} x_{align} \\ y_{align} \end{pmatrix} \right) - \begin{pmatrix} iP_x \\ jP_y \end{pmatrix} \quad (6.11)$$

with the alignment constants φ, x_{align}, and y_{align}, with the pixel pitch $\vec{P}$ and with the column i and row j position of the seed pixel. Equation 6.11 allows the calculation of residuals, seed charges and total cluster charges in dependence on the in-pixel hit $\vec{m}$.

Figure 6.19 shows the residuals of the DUT as a function of m_x and m_y. As anticipated in section 6.4.1, the residual and thus the intrinsic resolution worsens in the case of a central hit due to reduced charge sharing and improves with proximity to the pixel borders and subsequent increased charge sharing. This in-pixel dependence is a property of the PFA and sensitive to S/N and $\vec{P}$. This is effect expected[4] and observable in all DUT and telescope devices. The variation in x of the STD and C3G are both $\approx 0.6\mu m$, whereas the variation on the HiG is $\approx 0.2\mu m$. Here the small pitch of the STD ($P_x = 24\mu m; S/N = 128$) compensates for the improved S/N of the C3G ($P_x = 32\mu m; S/N = 148$) whereas the effect is reduced on the HiG since pitch and S/N are improved ($P_x = 20\mu m; S/N = 213$). The variation in y is on all devices $\approx 0.6\mu m$ which is unexpected and may be caused by incorrect treatment of the double-pixel structure with the η algorithm.

In figure 6.20 the in-pixel hit is extended to a double-pixel structure. It shows the shift of the residual distribution in x and y in dependence on the in-double-pixel point of passage m_x and m_y. A double-pixel structure is observable in the y shift of the residual distribution. Hits in the lower

[4] A detailed analytical caluculation is done in appendix B.

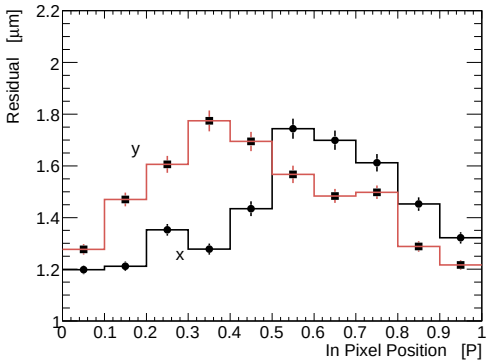

(a) STD

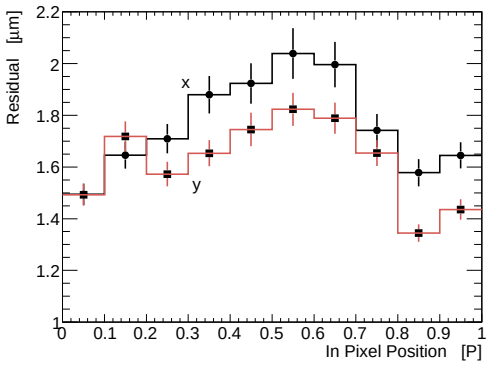

(b) C3G

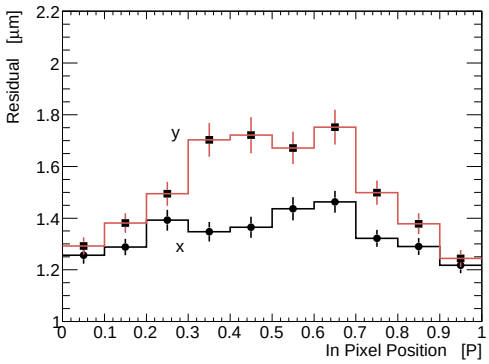

(c) HiG

Figure 6.19: Unbiased residuals in x (black) and y (red) in dependence on the in-pixel point of passage m through the DUT. The residual is largest in the center region of the pixel where the charge sharing and thus the S/N of the η value is minimal. The variation of the residual (and consequently the resolution) with m is an intrinsic property of a segmented detector and the reconstruction algorithm utilized. The point of passage is given in units of pixel pitch P of the devices accordingly (cf. section 4.4).

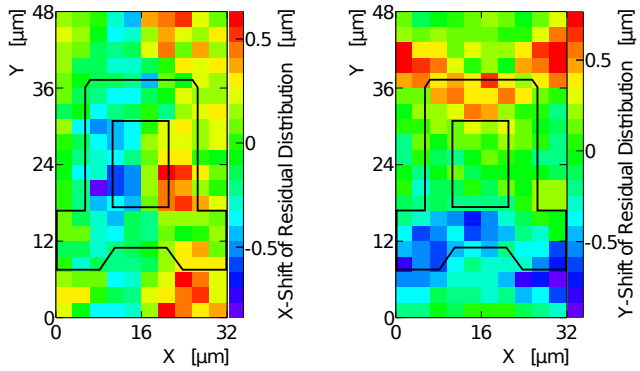

(a) Shift in x (b) Shift in y

Figure 6.20: Shift of residual distribution in x (a) and y (b) in dependence on the in-pixel point of passage $\vec{m} = (x, y)$ through a double-pixel of the telescope module Mod 11. The structure in (a) has a single-pixel pattern whereas (b) shows an apparent difference between odd and even pixels. Overlaid is the outline of the gate structure of the double-pixel.

part of the double-pixel, i.e. hits with the seed in a odd row, are reconstructed with a systematic bias towards low y and hits in the top pixel (seed row even) are shifted to higher y. The magnitude of this effect is in the order of $0.5\mu m$. Both effects, the variation of the residual as well as the dependence of the reconstruction bias on $\vec{m}$, is found on all modules. It is therefore likely that the figures 6.19 and 6.20 do not show inhomogeneities of the sensor but properties of the reconstruction, especially the position-finding algorithm. The double-pixel structure apparent in figure 6.20 (b) vanishes with the utilization of a η algorithm that considers the double-pixel structure as shown in [K$^+$09].

Figure 6.21 shows the cluster signal in dependence on $\vec{m}$ for the double-pixel structure of the three DUT. Although the cluster signal should be independent of $\vec{m}$ a significant variation of $\approx 6\%$ between the regions of the p^+ drain and n^+ clear implementations is observable in the STD. These variations in the charge collection efficiency are not as pronounced on the other sensors, which may be attributed to the properties of the device or to the limited statistics. Table 6.7 collects the minimum, average, and maximum values of the DUT cluster signal and the associated error[5]. The matrix inhomogenities in the micrometer scale are currently under

[5]The uncertainty has been estimated by bootstraping as shown in appendix D.

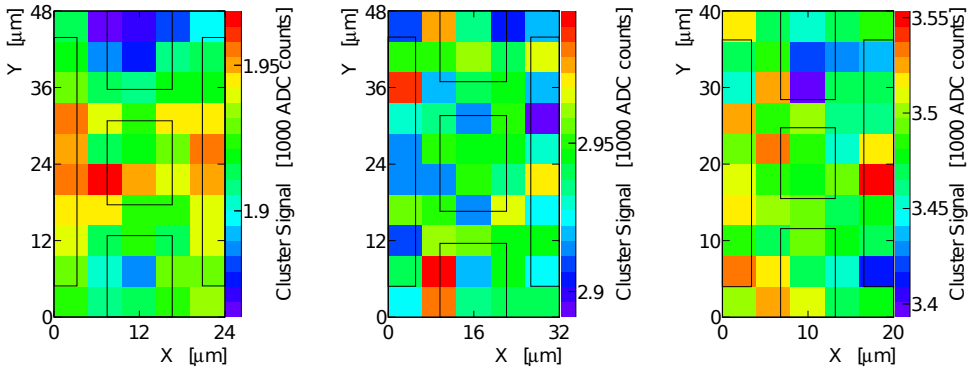

(a) STD (b) C3G (c) HiG

Figure 6.21: Total cluster charge in dependence on the in-pixel point of passage $\vec{m} = (x, y)$ through a double-pixel of the DUT. A 6% fluctuation between the drain and clear region is apparent in the STD. On the other devices the fluctuation is not significant and could be caused by the limited statistics. Overlaid are the outlines of the gate structures.

investigation by Reuen [Reu].

DUT	$Min(S)$	$\langle S \rangle$	$Max(S)$
STD	1860 ± 14	1920 ± 14	1960 ± 14
C3G	2900 ± 36	2940 ± 36	2990 ± 36
HiG	3410 ± 45	3480 ± 45	3530 ± 45

Table 6.7: Minimal, average and maximal cluster signals found in the in-pixel scan. The corresponding 2d-maps are shown in figure 6.21. All values are in units of ADC counts.

7 DEPFET Model Validation

The extensive analysis of the beam test data allowed a deep understanding of the sensor response to the passage of a MIP. This chapter will briefly explain a DEPFET model used as the digitizer stage of Monte Carlo (MC) studies to predict the performance of the Belle II vertex detector. This so-called *digitizer* simulates the response of the DEPFET sensor to a passage of high energy particles. Characteristic device parameters like the cluster signal or cluster size extracted from the beam test will be used to validate the digitizer.

7.1 Event Generation and Simulation

The goal of the simulation is to create a simple but accurate model that is able to describe the registered output of the DEPFET sensors in the Belle II vertex detector. The simulation of a particle's passage through the detector is split in two steps.

The interaction of the particle with the sensor bulk is simulated with the GEANT4 [A+03] based Mokka package. Within Mokka, the generated beam particles are tracked through the telescope volume (includes silicon sensors, air, and passive material) with so-called *G4-steps*. The energy loss, angular deviation, and particle species are saved to a G4-step for each interaction that creates secondary particles.

The digitizing stage picks up these G4-steps and simulates the charge collection in three steps. (1) The energy loss between two steps is converted to the number of signal electrons created which are then placed in grouped charge clusters called *ionization-points* over the length of the track segment between the two G4-steps. (2) As stated in section 5.6.1, the electric field is perpendicular to the surface in the bulk and only in the vicinity of the surface the influence of the deep-n doping pulls the charge sidewards into the internal gates. The latter aspect is ignored in the DEPFET model. With the knowledge of the drift field the time an electron needs to reach the surface, in dependence on the depth of the

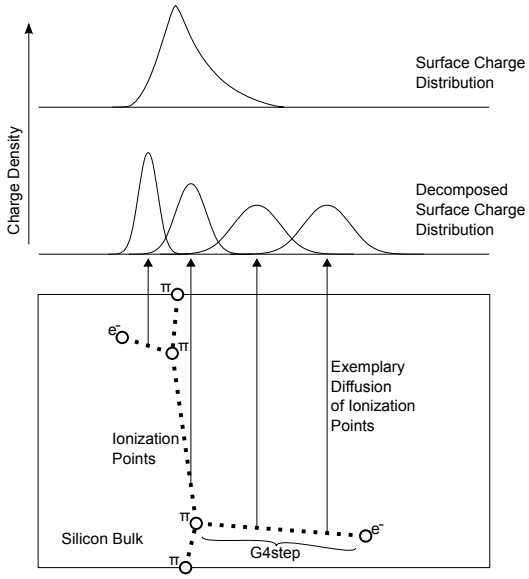

Figure 7.1: Scheme of the detector response simulation. A particle's passage is traced with G4-steps (open circles) through the sensor material. The energy loss along a G4-step is distributed in ionization-points (dots) along the corresponding track segment. Depending on the distance to the surface the drift time increases with depth and the diffusive spread widens (black arrows). The surface charge distribution is composed of the individual ionization-points after the lateral diffusive spread. The response of the detector is calculated as the integrated charge distribution over the pixel areas plus a Gaussian noise contribution (not shown).

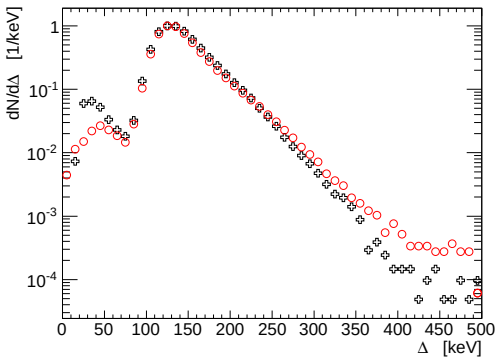

Figure 7.2: Comparison of the total cluster signal from the TB data (red circles) and from the MC digitizer (black crosses). The underlying samples include also clusters which are flagged "merged". The DEPFET model is able to reproduce the resulting low signal tail of the straggling function.

ionization-point, can be calculated [1]. In the digitizer model, this drift time is the single cause of lateral diffusion. Hereupon, the surface charge density is calculated as the sum of the individual ionization points after drift and diffusive smearing. (3) The output signal is determined as the charge density integrated over the area of the individual pixels plus a Gaussian noise contribution reflecting the amplification and sampling noise. A schematic representation of the simulation steps is shown in figure 7.1.

7.2 Model Validation

The accuracy of the digitizer can be tested if the produced detector signals are compared to the measured data from the beam test. The simulated event frames from the digitizer enter the analysis chain, as described in chapter 5, as pedestal-subtracted non-zero-suppressed events. Clustering, position-finding, and alignment are identical for the data and the MC sample. This equal treatment eliminates the systematic errors which would be introduced by comparing results from different analysis chains. To give one example: the systematic underestimation of the high energy deposits in the total cluster signal is mainly caused by the limitations of the fixed frame clustering and thus will appear during data as well as MC processing.

Figure 7.2 shows the total cluster signal from TB overlaid with the cluster signal from the MC sample. Both data sets include clusters that are flagged as merged (cf. section 5.5) during clustering which causes the over-expressed low signal tail of the straggling function (cf. section 6.2). The cluster charge from the digitizer output is in excellent agreement with the TB data in the peak region of the distribution. Even in the low energy regime the signals from the MC model retraces the contributions of merged clusters stemming mostly from δ-ray events. This further supports the thesis of this being a clustering artifact since the primary GEANT4 energy deposition has a vanishing value at $\Delta < 50keV$ and low energy clusters can only be a result of improper clustering.

In contrast to the total cluster signal, the seed signal strongly depends

[1] The electric field drifting the electrons to the structured sensor surface has been a matter of discussion in the last year. For simplicity the drift field has been taken as constant throughout the depth of the sensor similar to the field of a plate condenser. This approach has been refined by Schwenker [SGF10] who derives the bulk potential from the dopant concentration and the potentials applied in the sideward depletion scheme.

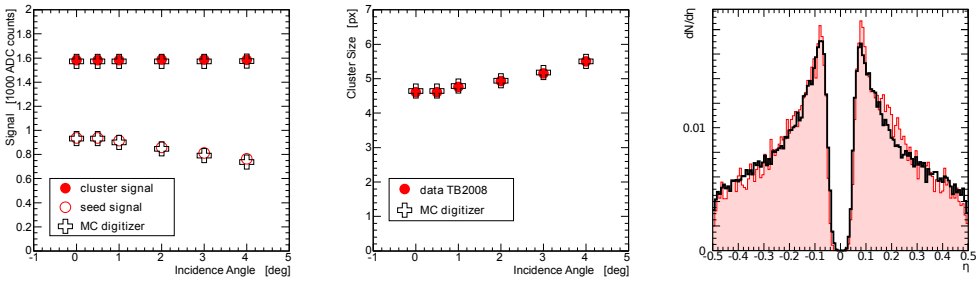

(a) MPV of cluster and seed signal in dependence on the incidence angle.

(b) Average cluster size in dependence on the incidence angle.

(c) η distribution from TB data and the prediction of the digitizer.

Figure 7.3: Comparison of experimental data to prediction of the digitizer. The red dots and filled histogram are extracted from the TB data. The black crosses and solid line correspond to the DEPFET model.

on the diffusive spread and the shape of the surface charge cloud. The seed charge can therefore be leveraged to test the diffusion model of the digitizer. Figure 6.5 (a) shows the MPV of the cluster and the seed signal extracted from the TB data and MC sample in dependence on the incidence angle of the particle beam. A four degree tilt results in a per mille elongation of the path length in the active material and the effect on the total cluster signal is negligible. However, the particle traverses a distance of $32\mu m$ parallel to the sensor surface distributing ionization charge along the way. This results in a reduced seed signal. The experimentally measured values of the cluster and seed signal are in good agreement with the predictions form the digitizer. A similar test is shown in figure 6.5 (b). The effect of the increase of distance traversed parallel to the surface with the angle is apparent in the increase of the mean cluster size. Although a detailed comparison of the cluster size reveals a differences of the distribution on the percent level, the average cluster size of TB data and MC sample are in good agreement. The third test to validate the digitizer is based on the comparison of the η distribution which also strongly depends on the surface charge cloud. Figure 7.3 (c) shows $\rho(\eta)$ from TB data overlaid with $\rho(\eta)$ obatined from the well performing MC digitization.

8 Conclusions

High precision vertex reconstruction is one of the key requirements to fully exploit the physics potential at future lepton colliders. The DEPFET active pixel sensor has been proposed as a candidate for the vertex detector in the ILC experiment. Furthermore, a pixel vertex detector for the Belle II experiment based on the DEPFET technology is currently under development and will be installed in 2014.

Within this thesis, the characteristics of three sensor prototypes for the ILC have been studied. The performance analysis has been based on a beam test conducted with ultra relativistic pions at CERN SPS. A tracking telescope has been employed to allow the measuring of position-sensitive device properties like the spatial resolution or the charge collection efficiency. The extensive analysis of the data allowed a deep understanding of the sensor response to the passage of an MIP and revealed subtle differences between the three prototypes tested.

Calibrating the detector response to the number of electrons created by the impinging particle in the sensor material allowed the determination of the internal gain of the prototypes. The new clear concept of the capacitive coupled clear gate as well as the reduction of the gate length showed a 36% and 81% increase in the internal gain, respectively. Measuring the signal-to-noise ratio of the $450\mu m$ thick prototypes allowed the estimation of the noise discrimination qualities of the planned $75\mu m$ thick sensors. Signal-to-noise ratios of up to 213 have been measured with the studied devices. Benchmark variables like signal-to-noise and residuals have been cross checked and verified by independent analysis.

Different position-finding algorithms have been compared according to their respective reconstruction precision. Algorithms that take the non-linear charge sharing between pixels into account have been proven to outperform other methods and were used to estimate the spatial resolution of the sensors. Furthermore, it has been proven that the resolution also depends on the degree of charge sharing. Average resolutions have been estimated and range between $1\mu m$ and $1.5\mu m$.

Inequalities in the response of the pixels observed in the previous sensor generation have been highly suppressed and the homogeneity of the

studied sensors has shown to be relatively smooth across the matrix of 64×256 pixels. With the introduction of additional potentials along the perimeter of the active area, field inhomogeneities could be tracked down as the cause of a reconstruction bias in the edge region of the sensor and allowed the reduction of this undesired effect.

Investigations of in-pixel properties showed a variation of the sensor response on the percent level. Unfortunately, sufficient statistics are only available for one prototype and further studies on the in-pixel charge collection efficiency need to be conducted. Furthermore, a reconstruction bias introduced by the inadequate treatment of the double-pixel structure by a position-finding algorithm that relies on a single-pixel periodicity has been observed. A mild improvement of the spatial resolution by utilizing an algorithm that incorporates the double-pixel structure is expected.

The comparison of measured responses to model predictions allowed the validation of a DEPFET model that will be used as a digitizing stage of Monte Carlo studies. The modeling of the potentials within the bulk is under ongoing refinement, but the minimal model presented in this work already shows excellent agreement with experimental measurements.

The DEPFET-specific additions implemented into the Marlin analysis framework will facilitate the timely and proper analysis of future beam test studies. To ensure the availability and the maintenance of the code, the changes to the EUTelescope processor compilation need to be reviewed and submitted to the official repository.

Overall, the DEPFET collaboration has proven that the outstanding intrinsic properties of the DEPFET sensor can successfully be implemented into a fully operational detector system with a superb signal-to-noise ratio and an excellent spatial resolution. Problems observed in previous generations have been addressed, while at the same time promising new modifications for new prototypes have been developed. One might be curious how the thinned Belle II devices with the new readout board will perform in the upcoming beam test in late 2010.

A Cross-Check of Residual Widths

In order to make the widths of the residual distributions of the DUT comparable to the results of the analysis done by Kodyš et al. an additional correction was applied to the HiG as well as to the telescope modules Mod 8 and Mod 9.

The results in table A.1, which were submitted to NIMA [A$^+$10c], have been obtained by a minor shift of the hit positions in dependence on the row of the seed pixel. A polynomial of degree seven has been fitted to the central region (16 <column< 240) of the function $\langle s \rangle (r_s)$, with the mean of the residual $\langle s \rangle$ and the position of the seed pixel r_s. The polynomial is used to correct for the wobble seen in the central region of figure 6.13 (b). The correction was applied in y direction only.

The correction has not been applyed in the analysis presented in chapter 6 since good results could be obtained from a clean sample of hits in the central region of the sensor. Therefore, the presented analysis represents a minimalistic procedure, which allows to assess the performance of the DUT without complex corrections for matrix inhomogenities.

The agreement of the values to the level of $0.1 \mu m$ is very good in consideration of the fact that there are subtle differences in the processing of the data. These differences include important steps like the alignment and the correction of matrix response inhomogeneities as well as the position finding, which is done by Kodyš et al. with a variation of the η algorithm that incorporates the double-pixel structure of the sensors.

Device	dir.	σ_G	σ_P
Mod 11	x	2.39	2.49
	y	2.24	2.28
Mod 4	x	1.52	1.60
	y	1.27	1.38
HiG	x	1.46	1.54
	y	1.42	1.42
Mod 8	x	1.81	1.98
	y	1.55	1.61
Mod 9	x	1.97	1.97
	y	1.60	1.61
Mod 5	x	2.86	3.24
	y	2.89	2.86

Table A.1: Results from fitting a Gaussian (μ, σ) (range: $\pm 10 \mu m$) to the unbiased residual distributions of all sensors in run 2285. The σ_G values are the results of the analysis presented here and σ_P are the results of the analysis performed by Kodyš et al. All values are in units of μm.

B Analytic Analysis of the η PFA

In the following the η algorithm will derived and its characteristics and limitations will be discussed.

B.1 Calculation of η

The signal collected in the pixel is the signal charge created in the silicon bulk that drifted within the electric field towards the surface. To derive the typical shape of the η function simplifications have to be made. First the particles trajectory is taken as straight and perpendicular to the detector surface. Furthermore, it is assumed that the signal charge is deposited continuously along the passage through the bulk. At last, the detector is treated as a plate condenser, i.e. the electric field is taken to be constant between the back contact and the structured surface. this leads to a constant drift speed of the signal electrons and an effective diffusion spread proportional to the drift length z. From this the charge density on the surface of the device can be calculated in dependence on the effective diffusion constant D, the in pixel hit position m and a lateral coordinate u for the one dimensional case:

$$\rho_{SC}\left(D, m, u\right) := \int_0^{450\mu m} A(D)\, \exp\left(-\frac{\left(u-m\right)^2}{2\, D\, z}\right) dz \tag{B.1}$$

The lateral coordinate can be replaced by $\sqrt{(x-m)^2+(y-n)^2}$ to transfer the problem to 2D and the integral can be solved analytically with the use of the incomplete gamma function γ (equation 6.5.2 in [AS72]). This leads to figure B.1 (a) and the following expression:

$$\begin{aligned}\rho_{SC}\left(D, x, y, m, n\right) = &- A'(D)\, \gamma\left(-\frac{1}{2}, \frac{(x-m)^2+(y-n)^2}{450\mu m\ D}\right) \\ &\cdot \sqrt{(x-m)^2+(y-n)^2}\end{aligned} \tag{B.2}$$

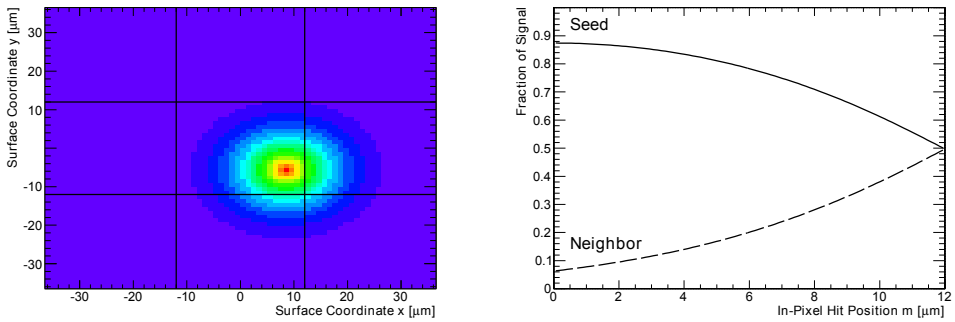

(a) Color map of surface charge cloud. The black lines represent the pixel boundaries. Purple indicates a low and red a high charge density.

(b) Fraction of signal collected in the seed and neighbor pixel as a function of the in-pixel point of passage.

Figure B.1: Calculated sensor response.

Since the hit reconstruction in x is independent of the hit position in y the surface charge cloud is integrated with respect to n over all possible in pixel hits. Furthermore, the seed signal is calculated via integration with respect to x and y over the pixel area.

$$S_S\left(D,m\right) = A''(D) \int_0^{p/2} dn \int_{-p/2}^{p/2} dx \int_{-p/2}^{p/2} dy\, \rho_{SC}\left(D,x,y,m,n\right) \tag{B.3}$$

The same integration is done for the neighbor signal with the different range in x.

$$S_N\left(D,m\right) = A''(D) \int_0^{p/2} dn \int_{p/2}^{3p/2} dx \int_{-p/2}^{p/2} dy\, \rho_{SC}\left(D,x,y,m,n\right) \tag{B.4}$$

These are the expressions for the average fraction of signal collected by the seed and highest neighbor pixel as a function of the x component of the in pixel hit position of the impinging particle. Figure B.1 (b) shows the graphical representation. From this the η value can be calculated for all $m \in [0, p/2]$:

$$\eta\left(D,m\right) = \frac{S_N}{S_N + S_S} \tag{B.5}$$

For a large set of hits the pixel area should be illuminated uniformly. This leads to the uniformity of the probability distribution of m. With

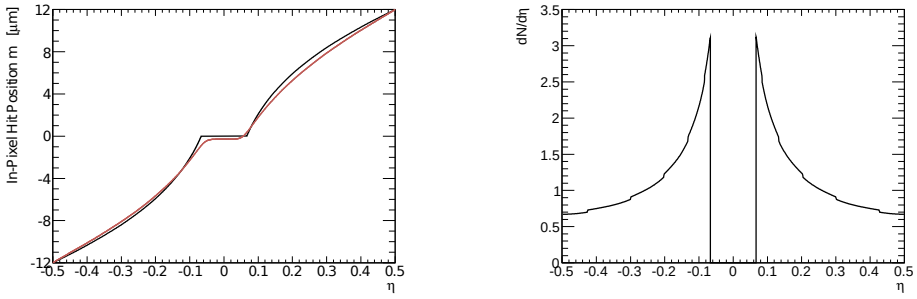

(a) Analytically calculated (black) and measured (red) η correction function.

(b) Analytically calculated η probability density. The small steps are numerical residues.

Figure B.2: Calculated η correction function and probability density for STD.

the use of equation B.5, this uniform probability in m can be transformed to the probability to find a certain η. η as a function of m and the eta probability density function are show in figures B.2.

B.2 Uncertainties in η

In this section, the the error (i.e. noise) in the pixel signal is propagated to estimate the optimal effective diffusion and to derive the lower resolution limit of the detector.

According to the Gaussian error propagation the error in η Δ_η, which results from the normalized noise Δ_{Px}, i.e. the quotient of the pixel noise and the MPV of the cluster signal, can be calculated to

$$\Delta_\eta(D,m) = \sqrt{\left(\Delta_{Px}^2\left(\frac{1}{S_N+S_S}-\frac{S_N}{(S_N+S_S)^2}\right)^2\right)+\left(\Delta_{Px}^2\left(\frac{S_N}{(S_N+S_S)^2}\right)^2\right)}, \quad \text{(B.6)}$$

which simplifies to

$$\Delta_\eta(D,m) = \frac{\sqrt{2}\,\Delta_{Px}}{(S_N+S_S)}\sqrt{\left(\frac{1}{2}-\frac{S_N}{(S_N+S_S)}\right)^2+\frac{1}{4}}. \quad \text{(B.7)}$$

For a given pitch P the optimal effective diffusion D is given by the condition that η averaged over m is minimal

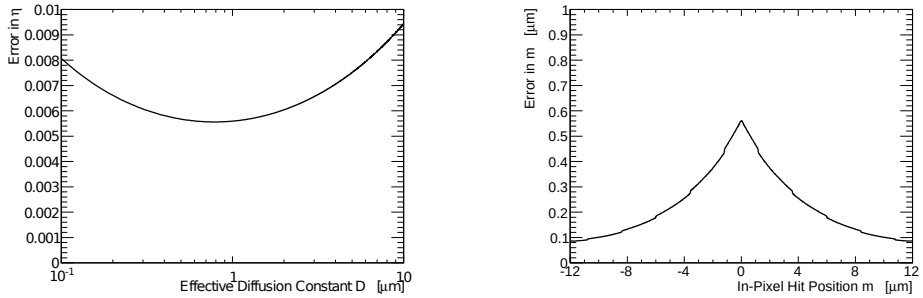

(a) Uncertainty in η as a function of the effective diffusion constant D. For STD D has been estimated to $3.6\mu m$.

(b) Error in the position-finding as a function of the in-pixel hit position m.

Figure B.3: Calculated error in position-finding for STD.

$$\frac{d}{dD}\int_0^{p/2} \Delta_\eta(D,m)\,dm \;=\; 0. \tag{B.8}$$

For a fixed D the lower resolution limit is estimated as a function of the in-pixel hit m through

$$\Delta_m(m) = \Delta_\eta(m)\,\frac{\partial}{\partial\eta} m(\eta(m)). \tag{B.9}$$

The error in η as a function of the diffusion D and the reconstruction precision limit Δ_m as a function of m is shown in the figures B.3.

C Development of EUTelescope

The following features have been added to the Marlin processors in the EUTelescope compilation:

- The *DEPFETReader* has been altered to save the start-gate position in the event header.
- The simple event viewer *DEPFETSimpleEventDisplay* has been developed. The processor allows dumping raw and pedestal corrected data frames to Root histograms.
- The algorithm for the calculation of the common mode noise in *EUTelPedestalNoiseProcessor* and *EUTelCalibrateEventProcessor* has been adapted to the requirements of the DEPFET sensors. The common mode can now be estimated as the median of a half double-row.
- The *EUTelClusteringProcessor* has been modified to output the cluster sizes of the fixed frame clusters depending on a selectable neighbor cut. Furthermore, the start-gate flag was introduced to mark clusters that contain cleared rows.
- *EUTelClusterFilter* has been modified to allow a proper pre-selection of clusters based on the seed or cluster signals of the different DUT and telescope modules. Prior to that the cut values could only be set globally.
- The position finding algorithms, other than CoG, explained in section 5.6 have been implemented into *EUTelHitMaker*.
- Dumping to Root NTuples was added to all relevant processors.
- Two new processors *DEPFETGainCorrectCalc* and *DEPFETGainCorrectApply* have been developed to calculate gain variations and apply corrections to the raw data.

D Additions to Gain Variation

The uncertainty in the measurements of gain (cf. section 6.6) and charge collection (cf. section 6.10) have been estimated by calculating the average signal from 1000 random samples with size n. The RMS of the resulting distribution, shown in figures D.1, is taken as the measuring error.

Figures D.2 show the gain modulation calculated from the average seed signal of the DUT and complement the results presented in section 6.6.

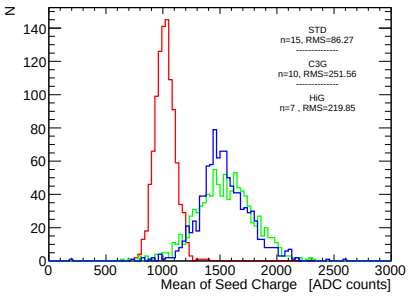

(a) Uncertainty in seed signal.

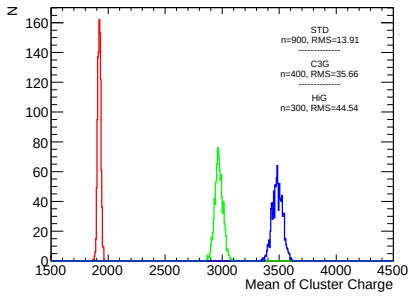

(b) Uncertainty in cluster signal.

Figure D.1: Uncertainty estimation of the mean value of the seed and cluster signals.

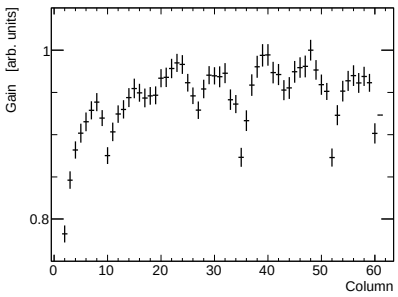

(a) Column-wise gain of STD

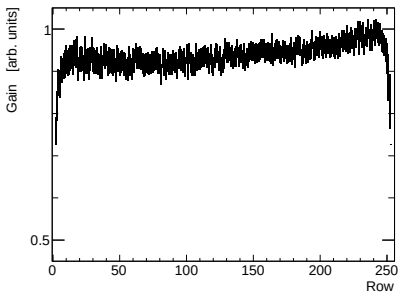

(b) Row-wise gain of STD

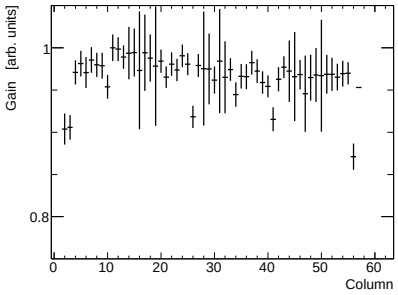

(c) Column-wise gain of C3G

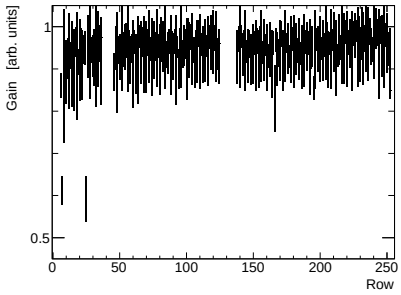

(d) Row-wise gain of C3G

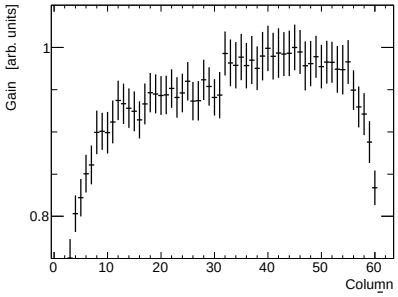

(e) Column-wise gain of HiG

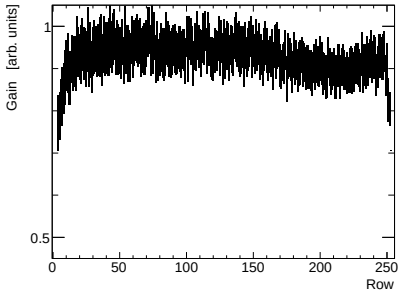

(f) Row-wise gain of HiG

Figure D.2: Gain modulation of DUT. Complementary plots to figure 6.10.

E Double-η Algorithm

The impact of a position-finding that includes the double-pixel structure of the DEPFET prototypes has been studied by calculating the η correction for odd and even rows separately. The difference of the η probability density for odd and even pixels is shown in figure E.1 (a), (c), and (d). Figures (b), (c), and (e) display the difference in the correction function. This difference accounts for a shift of maximal $0.07\mu m$ as compared with the single-pixel η algorithm, which is used in the analysis presented in chapter 6.

Reprocessing a data sample (run 2169) containing the STD DUT with this refined double-pixel η algorithm has shown no significant ($< 0.01\mu m$) improvement of the width of the residual distribution s and was therefore not used in the presented analysis. However, a significant improvement is expected with the use of a η algorithm that fully incorporates the double-pixel structure as explained in [Kod10].

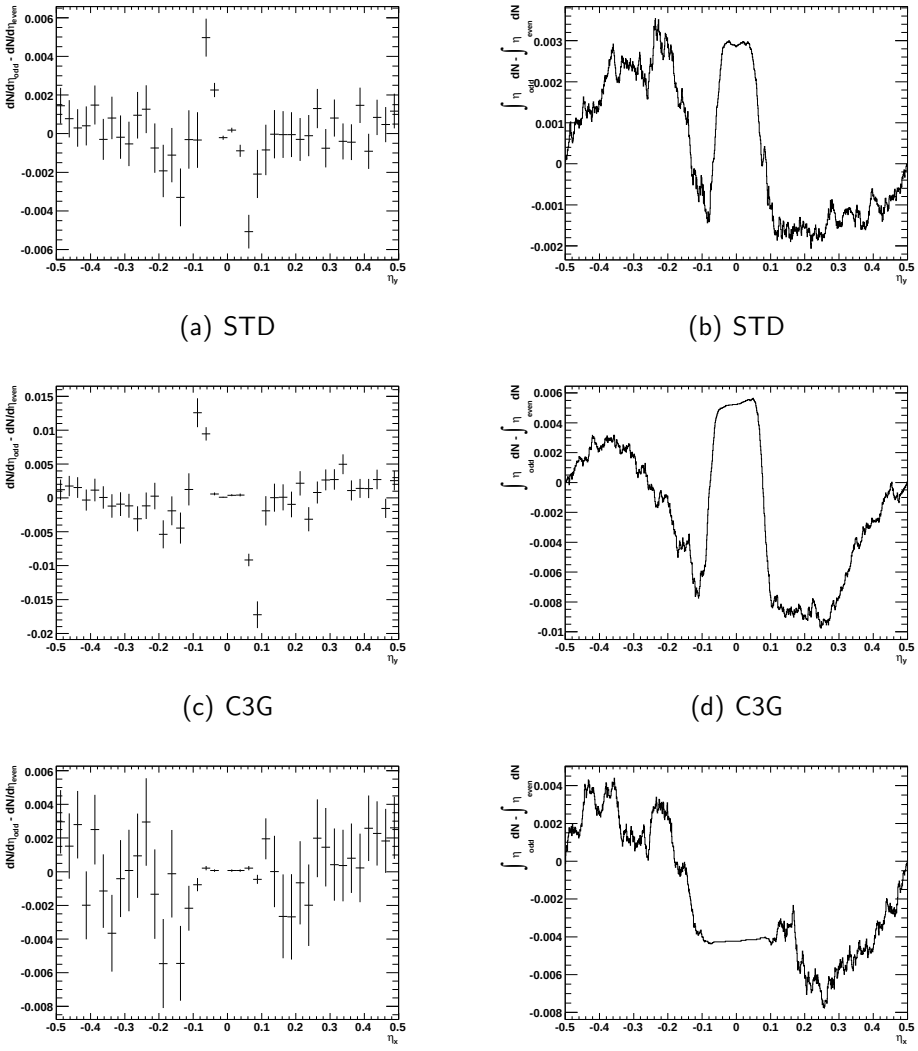

(a) STD (b) STD

(c) C3G (d) C3G

(e) HiG (f) HiG

Figure E.1: Difference in η values between odd and even pixel. The difference of the normalized (area set to unity) η_y distribution of odd and even pixel (left) and the difference in the integral $\int \eta_y dN$ (right) for the DUT. The integral $\int \eta_y dN$ is used as a look-up table for the position finding; the y value times the pixel pitch is a position (cf. section 5.6.3).

F Flowchart of Analysis Chain

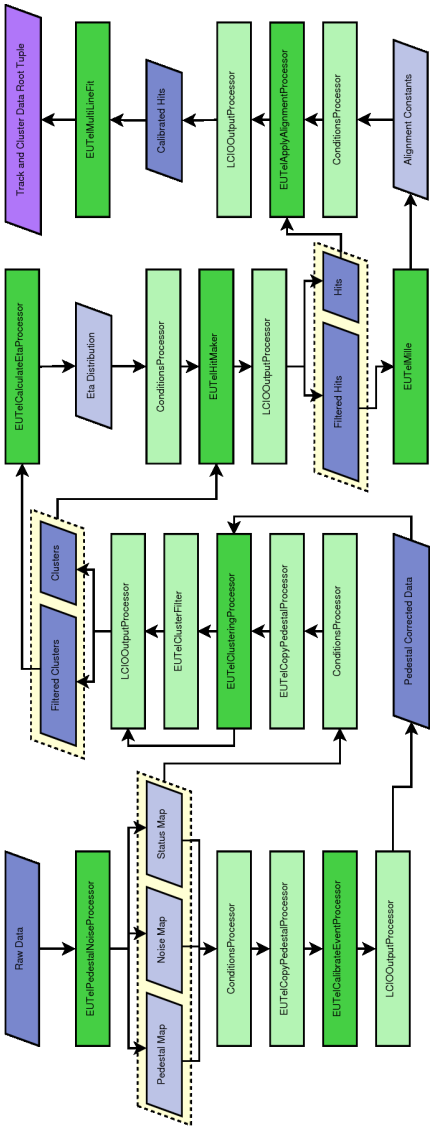

Figure F.1: Detailed flowchart of data processing analysis chain.

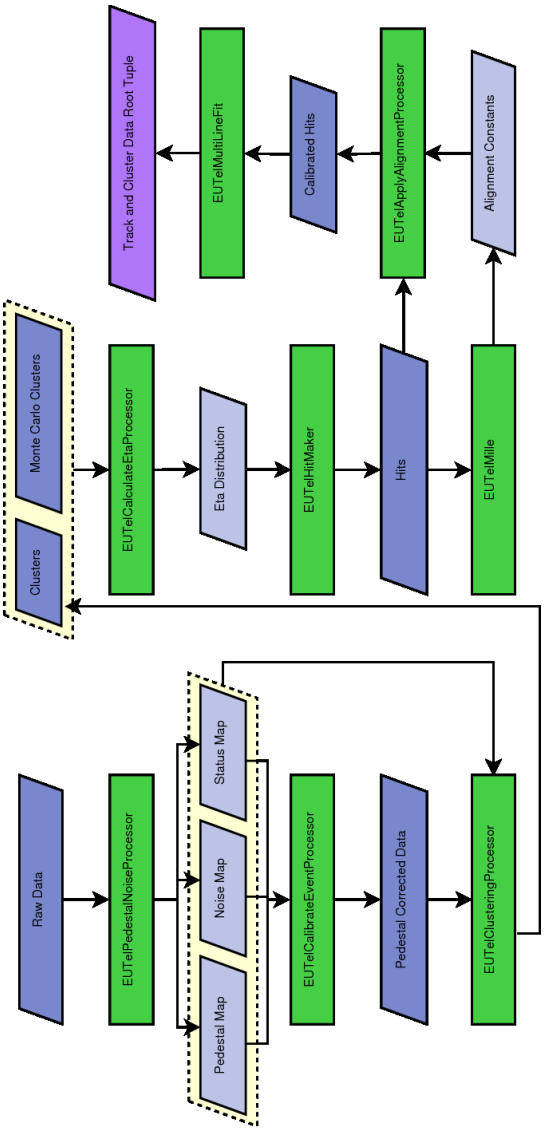

Figure F.2: Flow of data and MC analysis.

References

[A+03] S. Agostinelli et al. GEANT4: A simulation toolkit. *Nucl. Instrum. Meth.*, A506:250–303, 2003.

[A+04] L. Andricek et al. Processing of ultra-thin silicon sensors for future e+e- linear collider experiments. *IEEE Trans. Nucl. Sci.*, 51:1117–1120, 2004.

[A+08] C. Amsler et al. Review of Particle Physics. *Phys. Letters*, B667:1, 2008.

[A+10a] T. Abe et al. Belle II – Technical Design Report. *not yet published*, 2010.

[A+10b] Toshinori Abe et al. The International Large Detector: Letter of Intent. 2010.

[A+10c] L. Andricek et al. Intrinsic resolutions of DEPFET detector prototypes evaluated at beam tests. *Nucl. Instrum. Methods A*, not yet published, 2010.

[Ait69] D.W. Aitken. Energy Loss and Straggling in Silicon by High-Energy Electrons, Positive Pions, and Protons. *Phys. Rev.*, 179:393, 1969.

[All80] W.W.M. Allison. Relativistic Charged Particle Identification by Energy Loss. *Ann. Rev. Nucl. Part. Sci.*, 30:253–298, 1980.

[AS72] M. Abramowitz and I. A. Stegun. *Handbook of mathematical functions*. U.S. Government Printing Office Washingtor., D.C., 1972.

[AZ77] H.H. Andersen and J.F. Ziegler. *Hydrogen: Stopping Powers and Ranges in All Elements*. Pergamon Press, 1977.

[B+83] E. Belau et al. Charge collection in silicon strip detectors. *Nucl. Inst. Meth.*, (214):253 – 260, 1983.

[B+07a] James Brau, (Ed.) et al. ILC Reference Design Report Volume 1 - Executive Summary. 2007.

[B+07b] A. Bulgheroni et al. EUTelescope: tracking software. EUDET Memo 20, 2007.

[Bet30] H.A. Bethe. Zur Theorie des Durchgangs schneller Korpuskularstrahlen durch Materie. *Annalen der Physik*, 5:325, 1930.

[Bic83] H. Bichsel. Stopping power of M-shell electrons for heavy charged particles. *Phys. Rev.*, A28:1147–1150, 1983.

[Bic88] H. Bichsel. Straggling in thin silicon detectors. *Rev. Mod. Phys.*, 60:663, 1988.

[Bic06] H. Bichsel. A method to improve tracking and particle identification in TPC and silicon detectors. *Nucl. Instrum. Methods*, A562:154–197, 2006.

[Blo06] V. Blobel. Software alignment for tracking detectors. *Nucl. Inst. Meth. Res. A*, 566(1):5 – 13, 2006.

[Boh48] N. Bohr. Energy Deposition by Electron Beams and Îť Rays. *Dan. Mat. Fys. Medd.*, 18:No. 8, 1948.

[CCFT64] J. H. Christenson, J. W. Cronin, V. L. Fitch, and R. Turlay. Evidence for the 2π Decay of the K_2^0 Meson. *Phys. Rev. Lett.*, 13(4):138–140, Jul 1964.

[CHL+05] J. Charles, A. Höcker, H. Lacker, S. Laplace, F. R. Le Diberder, J. Malclés, J. Ocariz, M. Pivk, and L. Roos. CP violation and the CKM matrix: assessing the impact of the asymmetric B factories. *The European Physical Journal C - Particles and Fields*, 41:1–131, 2005. 10.1140/epjc/s2005-02169-1.

[DEP10] Depfet website. `http://www.depfet.org`, Sep 2010.

[Esc10] S. Esch. Auslese neuer DEPFET-Sensoren mit verbesserter Ansteuerung und charakterisierenden Messungen zu Antwortverhalten und Homogenität. Master's thesis, Rheinischen Friedrich-Wilhelms-Universität Bonn, 2010.

[Fan63] U. Fano. Penetration of Protons, Alpha Particles, and Mesons. *Ann. Rev. Nucl. Sci.*, 13:1, 1963.

[Fur10] S. Furletov. A system for characterization of DEPFET silicon pixel matrices and test beam results. *Nucl. Inst. Meth. Res. A*, A doi::10.1016/j.nima.2010.06.322, 2010.

[G+84] E. Gatti et al. Silicon Drift Chambers - First Results and Optimum Processing of Signals. *Nucl. Inst. Meth. Res.*, 226:129–141, 1984.

[GBGJ03] F. Gaede, T. Behnke, N. Graf, and T. Johnson. LCIO persistency and data model for LC simulation and reconstruction. *arXiv*, physics/0306114v1, 2003.

[Gru93] C. Grupen. *Teilchendetektoren*. BI-Wiss.-Verl., Mannheim, 1993.

[H+04] S. Hashimoto et al. Letter of Intent for KEK Super B Factory. *KEK Report*, Apr. 2004.

[HJM+83] S. Hancock, F. James, J. Movchet, P. G. Rancoita, and L. VanRossum. Energy loss and energy straggling of protons and pions in the momentum range 0.7 to 115 GeV/c. *Phys. Rev. A*, 28(2):615–620, Aug. 1983.

[ICR79] ICRU. Report 31 – Average Energy Required to Produce an Ion Pair, 1979.

[ICR84] ICRU. Report 37 – Stopping Powers for Electrons and Positions, 1984.

[ICR93] ICRU. Report 49 – Stopping Power and Ranges for Protons and Alpha Particles, 1993.

[Jac98] J.D. Jackson. Electromagnetic form factor corrections to collisional energy loss of pions and protons, and spin correction for muons. *Phys. Rev.*, D59:017301, 1998.

[K+05] R. Kohrs et al. Development of a Prototype Module for a DEPFET Pixel Vertex Detector for a Linear Collider. *IEEE Trans. Nucl. Sci.*, 52:1171, 2005.

[K+09] P. Kodyš et al. DEPFET Beam Test 2008 - Prague Analysis Report. DEPFET Collaboration Internal Document, 2009.

[Kie10] C. Kiesling. Neue Physik mit B-Mesonen. *Jahrbuch 2010 - Max-Planck-Institut für Physik*, 2010.

[KL87] J. Kemmer and G. Lutz. New Detector Concepts. *Nucl. Instrum. Methods A*, 253:365, 1987.

[KL+90] J. Kemmer, G. Lutz, et al. Experimental Confirmation of a New Semiconductor Detector Principle. *Nucl. Instrum. Methods A*, 288:92–98, 1990.

[KM73] Makoto Kobayashi and Toshihide Maskawa. CP-Violation in the Renormalizable Theory of Weak Interaction. *Progress of Theoretical Physics*, 49(2):652–657, 1973.

[Kob68] E.J. Kobetich. Energy Deposition by Electron Beams and δ Rays. *Phys. Rev.*, 170:391, 1968.

[Kod10] P. Kodyš. Data pre-processing for the Prague analysis of TB 2009. DEPFET Collaboration Internal Document, 2010.

[Koh08] R. Kohrs. *Development and Characterization of a DEPFET Pixel Prototype System for the ILC Detector*. PhD thesis, Rheinischen Friedrich-Wilhelms-Universität Bonn, 2008.

[Lan44] L.D. Landau. On the Energy Loss of Fast Particles by Ionisation. *J. Exp. Phys. (USSR)*, 8:201, 1944.

[Lut99] G. Lutz. *Semiconductor Radiation Detectors*. Springer Verl., Berlin, 1999.

[Mar10] Modular Analysis and Reconstruction for the LINear Collider. `http://ilcsoft.desy.de/portal/software_packages/marlin/`, Aug 2010.

[Reu] L. Reuen. *not yet published*. PhD thesis, Rheinischen Friedrich-Wilhelms-Universität Bonn.

[Rum09] S. Rummel. *Investigation of DEPFET as Vertex Detector at ILC*. PhD thesis, Technische Universität München, 2009.

[Sch08] K. Schmieden. Charakterisierung einer neuen Generation von DEPFET-Sensoren mit Hilfe eines Lasermesssystems. Master's thesis, Rheinischen Friedrich-Wilhelms-Universität Bonn, 2008.

[SGF10] B. Schwenker, C. Geisler, and A. Frey. DEPFET Pixel Digitizer - Status Report. DEPFET Collaboration Internal Document, 2010.

[Ste82] R.M. Sternheimer. Density Effect for the Ionization Loss of Charged Particles in Various Substances. *Phys. Rev.*, B26:6066, 1982.

[ZN07] A. F. Zarnecki and P. Niezurawski. EUDET Telescope Geometry and Resolution Studies. *ArXiv Physics e-prints*, March 2007.

List of Figures

List of Tables

Acknowledgments

In the first place, I would like to thank the collaboration for the careful preparation and the skillful conduct of the beam test. Specifically, Marcel, Sergey, Julia, Jochen, Simone, Johannes, Carlos, Jelena, Christian, and Benjamin. I know that this work would have been more troublesome if it were not for your experience. Furthermore, I am thankful for the productive cooperation with my colleagues in Praha. Namely, Peter Kodyš and Peter Kvasnička.

I would like to thank Heather, Kim, Florian, and Gerrit for their proofreading skills, mental support, and increasing the data-ink ratio.

I am grateful for the friendly and helpful atmosphere I experienced in the High Energy Physics group. I would like to thank Benjamin Schwenker for the vivid and fruitful discussions on which most parts of this work are based. Finally, I owe special thanks to Prof. Dr. Ariane Frey who not only gave me the opportunity to participate in a fascinating project, but whose subtle guidance made work a pleasure.